Identification of sudden stiffness changes in the acceleration response of a bridge to moving loads using ensemble empirical mode decomposition

H. Aied[a], A. González[a,*] and D. Cantero[b]

[a]*School of Civil, Structural, and Environmental Engineering, University College Dublin, Dublin 4, Ireland*

[b]*Roughan & O'Donovan Innovative Solutions, Arena House, Arena Road, Sandyford, Dublin 18, Ireland*

[*]Corresponding author: arturo.gonzalez@ucd.ie

Abstract

The growth of heavy traffic together with aggressive environmental loads poses a threat to the safety of an aging bridge stock. Often, damage is only detected via visual inspection at a point when repairing costs can be quite significant. Ideally, bridge managers would want to identify a stiffness change as soon as possible, i.e., as it is occurring, to plan for prompt measures before reaching a prohibitive cost. Recent developments in signal processing techniques such as wavelet analysis and empirical mode decomposition (EMD) have aimed to address this need by identifying a stiffness change from a localised feature in the structural response to traffic. However, the effectiveness of these techniques is limited by the roughness of the road profile, the vehicle speed and the noise level. In this paper, ensemble empirical mode decomposition (EEMD) is applied by the first time to the acceleration response of a bridge model to a moving load with the purpose of capturing sudden stiffness changes. EEMD is more adaptive and appear to be better suited to non-linear signals than wavelets, and it reduces the mode mixing problem present in EMD. EEMD is tested in a variety of theoretical 3D vehicle-bridge interaction scenarios. Stiffness changes are successfully identified, even for small affected regions, relatively poor profiles, high vehicle speeds and significant noise. The latter is due to the ability of EEMD to separate high frequency components associated to sudden stiffness changes from other frequency components associated to the vehicle-bridge interaction system.

Keywords: Ensemble empirical mode decomposition, damage detection, moving load, bridge accelerations, non-linear response

1. Introduction

Bridges are subjected to continuous structural deterioration caused by repeated traffic loading, aging and environmental conditions. The degree of deterioration needs to be monitored periodically in order to ensure structural safety. If damage is prevented at an early stage, maintenance works will be carried out as required and before the bridge can become damaged beyond repair. For this purpose, accelerations due to bridge vibrations induced by everyday traffic and environmental loading are commonly collected by structural health monitoring systems to capture dynamic characteristics of the bridge (i.e., frequencies and mode shapes). The latter is a popular way to identify, locate and quantify deterioration based on the principle that damage affecting the mechanical properties of the structure will change the dynamic properties of the structure and it will allow the bridge operator to take adequate action. These vibration-based methods typically require many sensors and long records to distinguish between true damage and deviations from the expected 'healthy' results that do not necessarily imply damage (i.e., due to forced vibration and environmental conditions) [1-3].

Still another approach (complementary, but not exclusive) to damage detection is the identification of an anomaly in the time history of the total structural response in forced vibration (i.e., static + dynamic) to the passage of traffic. Using signal processing techniques, which often combine frequency and time domains (such as wavelet analysis), a number of researchers have been able to locate an anomaly in the processed signal that can be related to damage and located in the bridge with respect to the position of the moving load. These approaches aim to identify and locate damage using less testing requirements in number of sensors and test duration than other level II damage detection methods such as those based on mode shape curvature. In the development of these approaches, difficulties in gathering data from a real bridge in both healthy and damaged states (or after and before repair) have motivated the use of numerical models for theoretical testing based on assumptions that sometimes can be unrealistic, i.e., assuming a linear response even for significant stiffness losses. While these numerical models are valid to illustrate a concept, they appear to be insufficient to challenge and validate a technique able to capture the initiation of damage before stiffness losses become unrealistically large (i.e., leading to section failure). For example, damage modelled as a sudden or gradual loss of stiffness in a portion of a bridge assumed to be permanent and respond in the linear elastic range for the test duration can be easier to capture (i.e., via a frequency change) than a non-linearity only revealed when the yielding point is exceeded at a specific section. The latter takes place within a narrow time window while the structural response remains unaltered outside this period. However, it would be obviously beneficial to identify the first signs of non-linearity before critical damage in the form of significant losses of inertia or cracking (leading to catastrophic failure in prestressed concrete sections) could take place.

Therefore, this paper focuses on developing an approach that will capture a non-linear behaviour (modelled as a brief stiffness change) from the acceleration response of a structure traversed by a moving load. The first question that arises is how to characterize a non-linear response. This has been addressed in a wide range of mechanical and civil engineering applications via methods such as the Continuous Wavelet Transform (CWT) [4, 5], Unscented Kalman Filter (UKF) [6, 7], Hilbert-Huang Transform (HHT) [2, 8-10] and others. The HHT utilises Empirical Mode Decomposition (EMD) to estimate the Instantaneous Frequency (IF) and the Instantaneous Phase (IP). EMD is used to separate the signal (e.g., acceleration) into Intrinsic Mode Functions (IMFs), that separate the frequency content of the signal. The lowest IMFs contain the part of the signal corresponding to the highest frequencies. Applications of the EMD method to nonlinear and non-stationary signals for wide range of signals from speech characterisation to ocean wave data have shown its versatility and robustness in detecting inconsistencies. Several authors have attempted to identify nonlinearity by applying EMD and HT to a nonlinear damaged structures [2, 11-13]. However, detractors of EMD argue its lack of physical meaning due to mode mixing in the IMFs. First introduced by Wu and Huang [14], Ensemble Empirical Mode Decomposition (EEMD) has been found to eliminate the mode mixing problem of EMD [15]. EEMD has only been recently applied to damage detection in a number of applications. For example, An, et al. [16] applies the EEMD with Hilbert transform to analyse the non-linear and non-stationary signal produced by faulty wind turbines. Zhang and Xie [17] test concrete samples using impact echo data for defects by applying the EEMD and find that the white noise amplitude needs to be significantly higher compared to other investigations due to the implications of strong surface waves. Zheng, et al. [15] are able to successfully implement a new method called Partly Empirical Mode Decomposition (PEEMD) to detect faulty signals with high frequency and non-linear and non-stationary components. Even though the method proves successful in decomposing the signal by eliminating mode mixing, it does not show significant improvements compared to EEMD.

By the first time, EEMD is applied here to the acceleration response of a structure to a moving load to detect a sudden stiffness change. Accelerations are the subject of investigation as they are relatively easy to measure on the field and commonly used for monitoring purposes. Acceleration is a global load effect, as opposed to strain, where the measurement location needs to be at or nearby the damaged location to be able to perceive the damage. In this paper, the stiffness change is introduced using a bi-linear moment-curvature relationship in two types of Finite Element Models (FEMs): a 1-D beam and a 2-D plate. For clarity, the advantages and drawbacks of employing EEMD are discussed first using the simulations of the response of

the beam FEM to a moving load and compared to other techniques such as wavelet analysis [4, 5] and EMD [18] which have been used in a similar context in the literature. Second, EEMD is tested using the accelerations of a plate FEM traversed by a sprung vehicle with different damage extent, road roughness, vehicle speed and noise.

2. Application of EEMD to damage detection using the acceleration response of a beam to a moving load

This section uses a relatively simple discretized beam FEM traversed by a moving constant load to illustrate the feature in the total acceleration response that denotes non-linearity and how it is captured by a signal processing technique. A more sophisticated vehicle-bridge interaction (VBI) simulation model is employed in further sections, but it is avoided here as it may hinder characteristics of the damage feature to be highlighted. Damage can be detected once it has occurred or as it is occurring, i.e., cracking that causes a stiffness loss will remain with the structure as long as repairs (or further deterioration) do not take place. A far more challenging task is to detect damage before a deterioration sign such as cracking is visible, namely, when the yielding point is exceeded. The duration of the time window where the section enters a plastic range may be very short and it needs to be captured as it is occurring (Outside this window, a linear elastic stress-strain curve will apply again). Unless the section was very brittle, an element will exceed the elastic range before approaching failure [19, 20], and in this window, the affected element will respond in the elasto-plastic range [21]. In the case of composite structures, the yielding of steel gives a non-linear nature to the response that affects the response and dynamic characteristics of the structure. In reinforced concrete bridges, concrete will typically crack before steel yields, whereas in prestressed concrete bridges, concrete cracking must be prevented. Therefore, the acceleration response to a moving load is simulated for a beam with a localised elasto-plastic response. This acceleration is processed then using wavelet analysis, EMD and EEMD to compare their ability to capture brief stiffness changes in an element of the beam.

2.1 Simulation of the response of a beam finite element model to a moving load

The bridge is modelled as a 15 m simply supported beam model discretised into 30 elements (Fig. 1). Each element has two nodes and each node consists of 2 Degrees of Freedom (DOFs): vertical displacement and rotation.

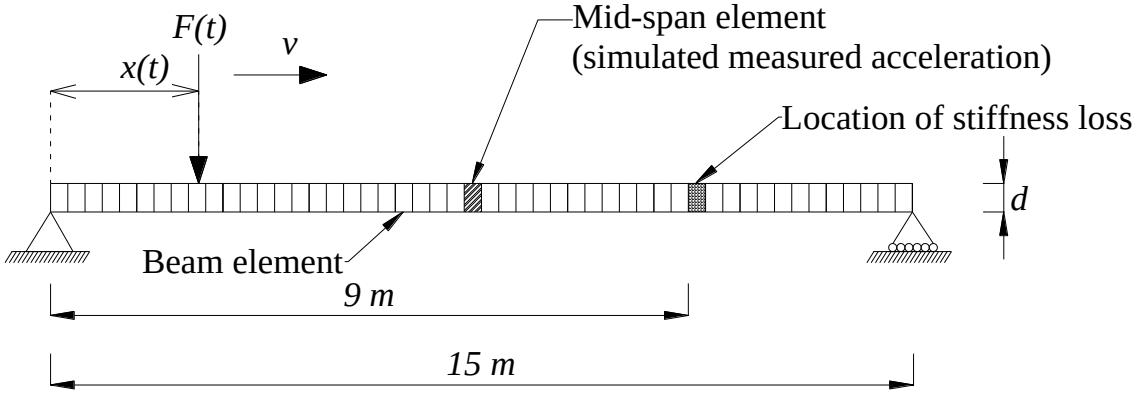

Fig. 1. Simulation model for a moving load on a beam

The beam cross-section is assumed to be rectangular with 12 m of width and 0.8 m of depth which are typical dimensions for the selected span [22]. Modulus of elasticity (E) and unit weight are assumed to be 31×10^9 N/m^2 and 2400 kg/m^3 respectively. The longitudinal stiffness (EI where I is inertia) of the beam is 1.59×10^{10} Nm^2 that combined with a mass per unit length of 23040 kg/m leads to 1st, 2nd and 3rd natural

frequencies of 5.8, 23.2 and 52.2 Hz respectively. The damping ratio is taken to be 2% [23, 24]. The moving load is idealized as a single constant force of 162 kN travelling at 20 m/s. The response of the simply supported discretized beam FEM traversed by a moving load is governed by the Equation of motion (1):

$$[M]\{\ddot{u}(t)\}+[C]\{\dot{u}(t)\}+[K]\{u(t)\}=\{F(t)\} \tag{1}$$

where [*M*], [*C*] and [*K*] are the global mass, stiffness and damping matrices respectively, {*F*(*t*)} is a vector representing the moving load on the beam (which varies on location and it is shared differently between the DOFs of the bridge at each point in time) and $\{\ddot{u}(t)\}$, $\{\dot{u}(t)\}$, and $\{u(t)\}$ are vectors containing the acceleration (m/s^2), velocity (m/s) and displacement (m) respectively of the DOFs of the beam at time *t*. The moving load is distributed to the degrees of freedom of the element that it is acting on, as a product of the hermite shape functions [25]. The latter allows replacing a force acting between nodes by an equivalent system of forces and moments acting at the element nodes. The incremental time step (Δt) is 0.001 s (i.e., a sampling frequency of 1000 Hz) in all the simulations.

A Euler-Bernoulli beam element is employed where the forces and moments at each beam node are related to the respective displacements and rotations by the elementary stiffness matrix [K_e] given in Equation (2). The global stiffness of matrix [*K*] is formed by assembling the stiffness matrixes [K_e] for all beam elements.

$$[K_e]=\begin{bmatrix} c & b & -c & b \\ b & a & b & \frac{a}{2} \\ -c & -b & c & -b \\ b & \frac{a}{2} & -b & a \end{bmatrix} \tag{2}$$

where $a = 4EI/L$, $b = 6EI/L^2$ and $c = 12EI/L^3$ form the elemental stiffness matrix. *E* is the Young's modulus (N/m^2), *I* is the moment of inertia (m^4) and *L* is the length of the element (m) (*L* = 0.5 m here). Equation (1) is then integrated using a Wilson-Θ scheme, to obtain the acceleration response at mid-span (i.e., at 7.5 m from the left support). Deviations in the structural response from a 'healthy' state (i.e., perfectly elastic) can be modelled by introducing changes in the stiffness matrixes of those beam elements deemed to have experienced some form of stiffness loss. The element selected to experience yielding is assumed to be located at 9 m from the left support, and its stiffness *EI* is determined using a bi-linear hysteretic moment-curvature relationship [26-28]. As a result of this model, the mechanical properties of the bridge (i.e., stiffness distribution and frequencies) will vary if the yielding point is exceeded at the selected element, but only for a short period of time. The aim of this model is testing EEMD in its ability to capture non-linearity (which can be prelude of damage) as it is occurring given that it will become unappreciable outside this period. It is acknowledged that surpassing the yielding point and entering the elasto-plastic range is not necessarily critical for a structure.

Fig. 2 shows the bi-linear hysteretic model employed here which interrupts the linear response found up to the yielding point. This model has been found to provide close results to reality [29], and for simplification purposes, it is preferred over more complex non-linear representations of stiffness loss such as Bouc-Wen [30] or the model by Kikuchi and Aiken [31]. Fig. 2 allows obtaining the stiffness *EI* of the element to include in the elementary stiffness matrix (Equation (2)) from the moment-curvature relationship (*M* - Φ). The bi-linear hysteresis can be separated into a linear component (Fig. 2(b)) and an elasto-plastic component

(Fig. 2(c)). In Fig. 2(a), the slope of the moment-curvature relationship is described by the stiffness (a = 4EI/L) up to the yielding point. Hysteresis relationships for parameters in Fig. 2(a) can be found in the literature [26, 30, 32, 33]. In Fig. 2(b), p is the stiffness apportioned to the linear component and in Fig. 2(c), q is the stiffness apportioned to the elasto-plastic component (q = 1 - p). M_p is the yielding bending moment where change in stiffness occurs. The level of post-yield stiffness loss is determined by p [34].

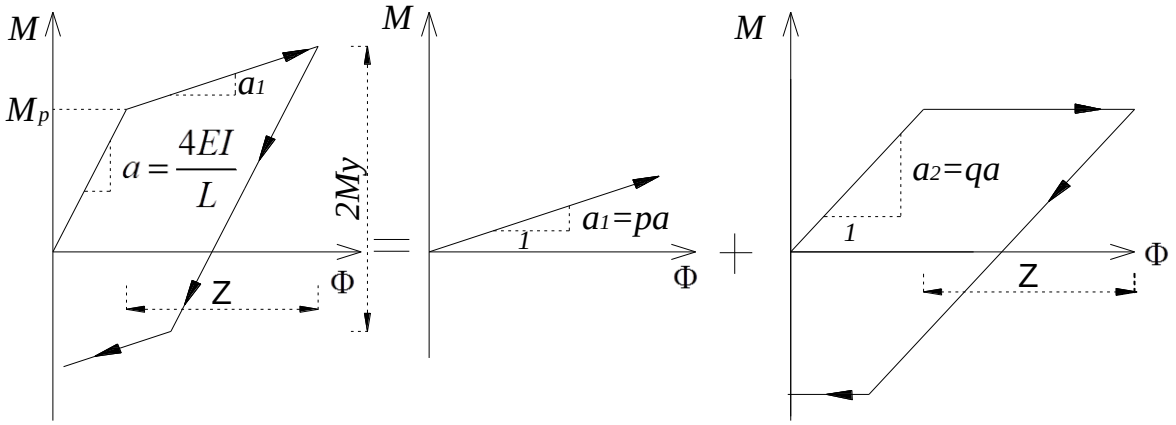

(a) (b) (c)

Fig. 2. Bi-linear moment-curvature relationship: (a) Bi-linear hysteresis relationship; (b) Linear component; (c) Elasto-plastic component

The hysteretic bending moment M is related to curvature Φ by [25]:

$$M(j,t) = p \times EI(j,t) \times \Phi(j,t) + (1-p) \times EI(j,t) \times Z(j,t) \tag{3}$$

where $EI(j,t)$, $\Phi(j,t)$ and $Z(j,t)$ are the stiffness (or modulus of elasticity by second moment by area), curvature and hysteretic curvature respectively at element j and time t. $Z(j,t)$ is calculated using:

$$Z(j,t) = Z(j,t-1) + \dot{Z}(j,t) \times \Delta t \tag{4}$$

where Δt is the incremental time step and $\dot{Z}(j,t)$ in Equation (4) is obtained from:

$$\dot{Z}(j,t) = \dot{\Phi}(j,t)\left[H_3(\dot{\Phi}(j,t)) \times H_4(Z(j,t-1) - \Phi_y) + H_2(\dot{\Phi}(j,t)) \times H_1(Z(j,t-1) + \Phi_y) \right] \tag{5}$$

In Equation (5), $\dot{\Phi}$ is the rate of change in curvature with time (i.e., $\dot{\Phi}(j,t) = \frac{\Phi(j,t) - \Phi(j,t-1)}{\Delta t}$), and H_1, H_2, H_3 and H_4 are the Heaviside's unit step functions given by:

$$H_1(\Phi) = \begin{cases} 1, \text{ for } \Phi \geq 0 \\ 0, \text{ for } \Phi < 0 \end{cases}$$
$$H_2(\Phi) = \begin{cases} 0, \text{ for } \Phi \geq 0 \\ 1, \text{ for } \Phi < 1 \end{cases} \quad (6)$$
$$H_3(\Phi) = \begin{cases} 1, \text{ for } \Phi > 0 \\ 0, \text{ for } \Phi \leq 1 \end{cases}$$
$$H_4(\Phi) = \begin{cases} 0, \text{ for } \Phi > 0 \\ 1, \text{ for } \Phi \leq 1 \end{cases}$$

Note that $\dot{\Phi}$ is positive when Φ is increasing and $\dot{Z}$ is equal to either zero or $\dot{\Phi}$ when the system is in sliding mode or non-sliding mode respectively. The yield curvature, Φ_y, is related to the yield moment, M_p, by:

$$\Phi_y = \frac{M_p}{EI} \quad (7)$$

The values adopted for p and q in the simulations are 0.51 and 0.49 respectively [33]. For a value of $p = 1$ the M - Φ (moment-curvature) relationship is linear, and for $p = 0.51$, a bilinear hysteresis relationship is formed where the slope a_1 is 51% of the slope a (Fig. 2). In other words, if M_p is exceeded, there is 49% loss in stiffness for a short period of time. Only within this period, the healthy bridge frequencies of 5.8, 23.2, 52.2 Hz are transformed into 5.71, 23.0 and 51.6 Hz respectively. At unloading the curve returns to the original value (slope a) and the bridge returns to vibrate at frequencies in the elastic range.

Fig. 3 shows the mid-span acceleration response due to the moving load for two cases: a perfectly elastic beam and a beam with an element susceptible to an elasto-plastic response at 9 m. The horizontal axis represents the time from the instant that the load enters the beam. A Power Spectral Density (PSD) analysis of Figs. 3(a) and (b) provides the same peak for a frequency of about 5.8 Hz. Only in the time domain it is possible to appreciate a disturbance between 0.39 to 0.45 s in Fig. 3(b) that did not occur in the linear case of Fig. 3(a).

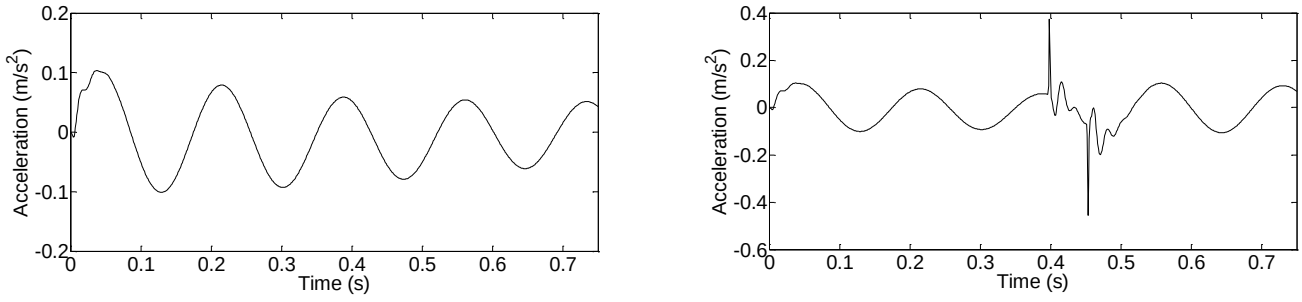

(a) (b)

Fig. 3. Mid-span acceleration to a moving load versus time for: (a) a perfectly elastic beam; (b) a beam with a localised elasto-plastic response at 9 m

The stiffness of the selected element varies during the load crossing as a result of the adopted bilinear hysteretic model. The vertical axis of Fig. 4 represents the true stiffness ratio (defined by actual stiffness divided by the stiffness in the elastic range) versus time for the section at 9 m. As expected, the stiffness loss takes place at the same time interval where a disturbance is appreciated in Fig. 3(b). The load will be over

the element susceptible to an elasto-plastic response at 0.45 s (= 9/20), but as the load approaches the elasto-plastic element, i.e., at 0.39 s, the moments have got sufficiently large as to exceed the yield point.

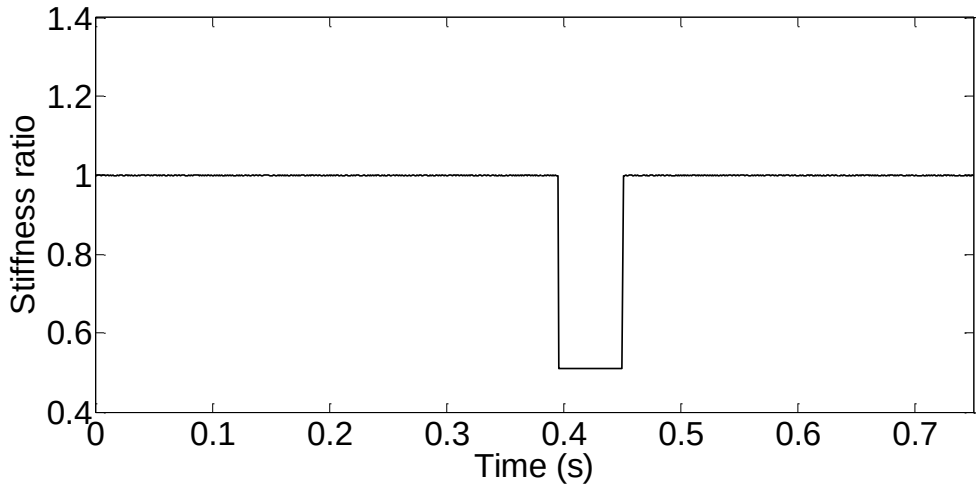

Fig. 4. Variation of stiffness ratio for section at 9 m with time corresponding to response in Fig. 3(b)

The question to be addressed next is: "Can sudden stiffness changes in this element be detected from the mid-span time-history acceleration using a signal processing technique?"

2.2 Identification of Stiffness Changes Using Wavelets, EMD and EEMD

2.2.1 Wavelet analysis

The contour plot of Fig. 5(a) is obtained from applying wavelet analysis based on the Mexican Hat to the acceleration signal of Fig. 3(b). This contour plot can be exploited to locate damage from the simulated response of a structure traversed by a moving load as tested first by Zhu and Law using displacements [35] and then by Hester and Gonzalez using accelerations [4]. These authors show that damage can be located within the total acceleration at lower speeds, however, at moderate speeds as the one tested here, the narrowing of the signal and edge effects make difficult to distinguish the damaged area. Here, the loss in stiffness between 0.39 and 0.45 s is only identified at low scales from 1 to 10, corresponding to frequencies from 250 to 25 Hz respectively. The scale of 10 is compared to a beam with a fully elastic response in Fig. 5(b). Although a comparison of the wavelet coefficients with elasto-plastic response to those with an elastic response reveal the time instant at which stiffness varies, the duration is unclear (i.e., from 0.39 to 0.45s as shown in Fig. 4). It must be acknowledged that the use of more complex simulation models containing high frequency components and noise will affect the wavelet coefficients for low scales, and it will become even more difficult to establish the instance and duration of a stiffness change occurrence.

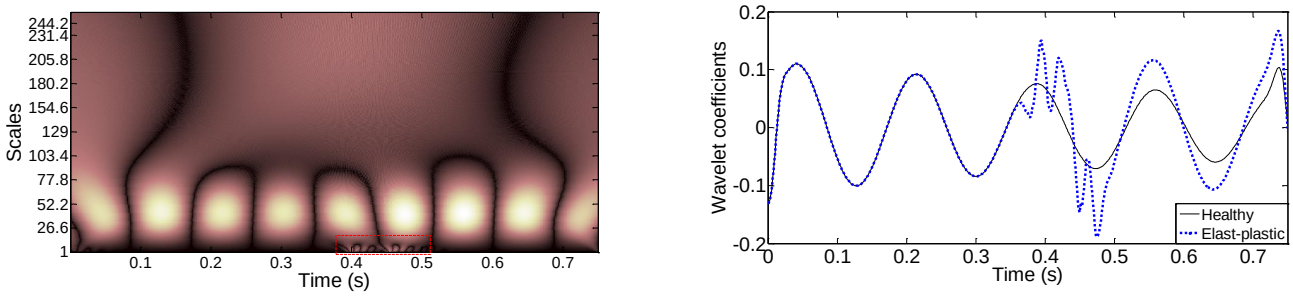

(a) (b)

Fig. 5. Wavelet analysis of mid-span acceleration in forced vibration (Fig. 3(b)) of a beam with an elasto-plastic response at 9 m (between 0.39 and 0.45 s): (a) contour plot of wavelet coefficients versus time and

scale; (b) Comparison of wavelet coefficients for a scale of 10 in the case of a perfectly linear elastic beam ('healthy') and a beam with a localised elasto-plastic response at 9 m

To improve the sensitivity of a wavelet-based damage detection algorithm, Hester and Gonzalez [4] use the average wavelet energy content for equally spaced strips along the bridge (i.e., taking into account many scales). Although they address the singularities at the start and the end of the processed signal by trimming the original signal, they acknowledge the algorithm is not as effective when the speed of the vehicle increases and the bridge span decreases (i.e., the signal gets shorter and the impact of edge effects becomes more prominent).

An inconvenience of the wavelet approach is related to the need to select: (1) a mother wavelet which is unknown *a priori*, given that some may work better than others in capturing a specific damage, and (2) a scale away from the bridge frequency, which may be corrupted by multitude of other frequencies, including noise.

2.2.2 EMD

EMD is an adaptive empirical method that removes the need for selecting a mother wavelet or a specific scale in a wavelet-based approach. In the EMD process the signal is decomposed into a number of IMFs using the 'sifting' process. The IMFs can be defined as a counterpart to the simple harmonic function representation, but instead of having a constant amplitude and frequency these are variable and time-dependant. The IMFs must satisfy two conditions: (a) the number of extrema and the number of zero crossings must differ by not more than one, and (b) the mean value of the envelope defined by the maxima and the minima at any given time must be zero. The EMD to obtain the IMFs is illustrated in Fig. 6.

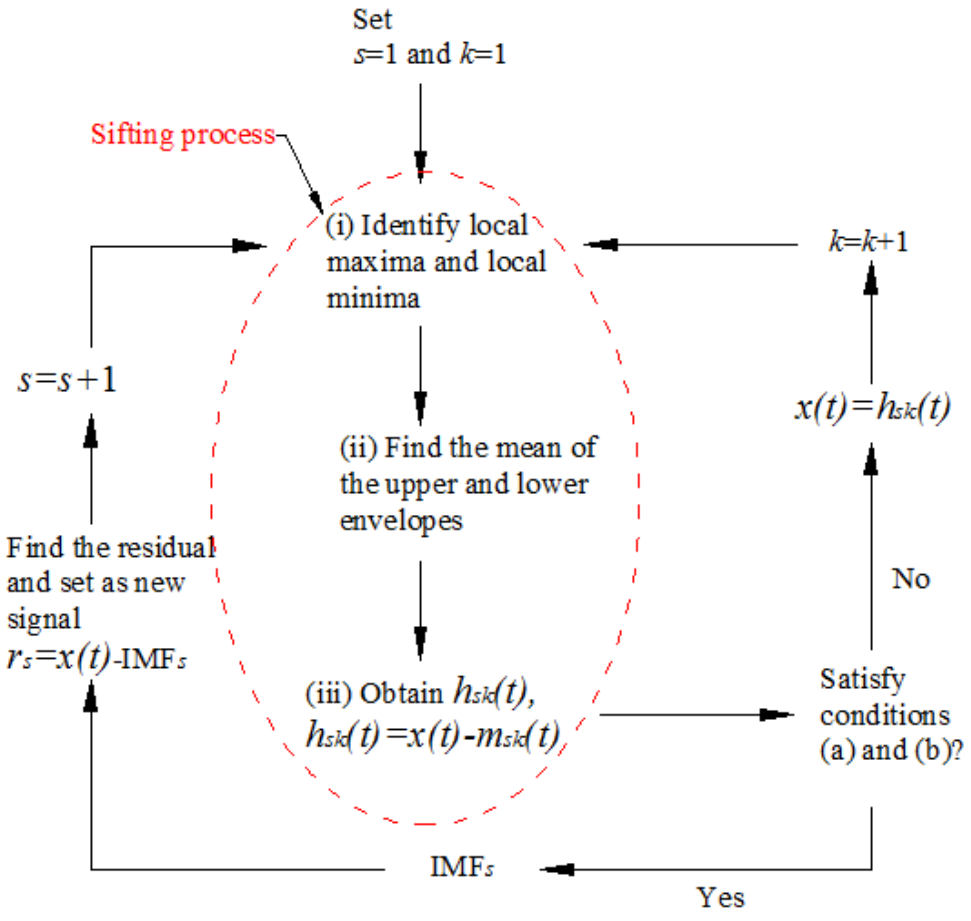

Fig. 6. Schematic of the EMD process

In Fig. 6, $x(t)$ is the original data set, $m_{sk}(t)$ is the mean of the upper and lower envelopes of the signal for the s^{th} extracted IMF and k^{th} sifting process. The first $h_{sk}(t)$, i.e., $h_{11}(t)$, rarely satisfies the two conditions for an IMF and therefore the process is repeated with $h_{11}(t)$ being treated as the signal, i.e., $h_{11}(t) = x(t)$. The first IMF is obtained when the aforementioned (a) and (b) conditions are met for some $h_{1k}(t)$ after the sifting process has taken place a number of times k resulting into:

$$\begin{aligned} h_{1k}(t) &= h_{1(k-1)}(t) - m_{1k}(t) \\ c_1(t) &= h_{1k}(t) \end{aligned} \tag{8}$$

where $c_1(t)$ (or $h_{1k}(t)$) is the first IMF. The process of sifting separates the finest local mode from the data first. In order for the IMF to have a physical meaning of amplitude and frequency modulation there needs to be criteria for the sifting process to stop (i.e. stoppage criteria for how many times the signal is sifted). Separating the first IMF from the rest of the data gives the residual ($r_1(t) = x(t) - c_1(t)$) from the first IMF. The residual is used as the input to calculate the second IMF ($c_2(t)$) and the decomposition process is repeated S times until the value of $r_s(t)$ becomes a monotonic component from which no more IMFs can be extracted. Specifically, the normalised squared difference between two successive sifting operations (s) and (s+1) needs to be small. In this paper, the stoppage criteria of the sifting process, k-numbers, is based on the method by Huang, et al. [8] which states that the sifting process only stops after the number of zero crossings and number of extrema are (1) equal or at most differ by one and (2) stay the same for S consecutive times. Extensive tests by Yang, et al. [36] suggest that the optimal value of S is between 4-8 [10].

EMD-based damage detection algorithms rely on the principle that a sudden loss in stiffness in a structural member will cause a disruption in an otherwise smooth response that can be detected through a distinctive spike in the IMF. The IMFs with higher frequency components are more sensitive to this disruption. Some authors have proven that a sudden drop in stiffness can be located in time as it is occurring via this distinctive spike using EMD, i.e., applied to the accelerations of a building subjected to earthquake excitation [37]. The spike in the IMF can be used to locate the affected region either in time – when damage occurs – or in space – where damage occurs –. The EMD is applied to the acceleration signal in Fig. 3(b) and four IMFs are extracted ($c_1(t)$ to $c_4(t)$) as shown in Fig. 7. The two IMFs with highest frequency content, i.e., $c_1(t)$ and $c_2(t)$, indicate via a series of peaks, the time instant of 0.39 s at which stiffness loss occur and its duration (approx. 0.06 s) before the stiffness returning to normal. However, there are other peaks of magnitude as high as or even higher than those occurring at the time of change in stiffness for a given IMF. While there are signs of the elasto-plastic components between 0.39-0.45 s, EMD is unable separate the 'healthy' (or perfectly elastic) components of the acceleration signal clearly from the elasto-plastic ones as a consequence of mode mixing. The latter is a major drawback of EMD, leading to an IMF either made of signals with widely disparate frequencies or a signal of sinusoidal frequency residing in different IMF components. When mode mixing occurs, an IMF can cease to have physical meaning, suggesting falsely that there may be different physical processes represented in a mode. Mode mixing appears more clearly in the EMD representation of the response of complex simulation models with many frequency components.

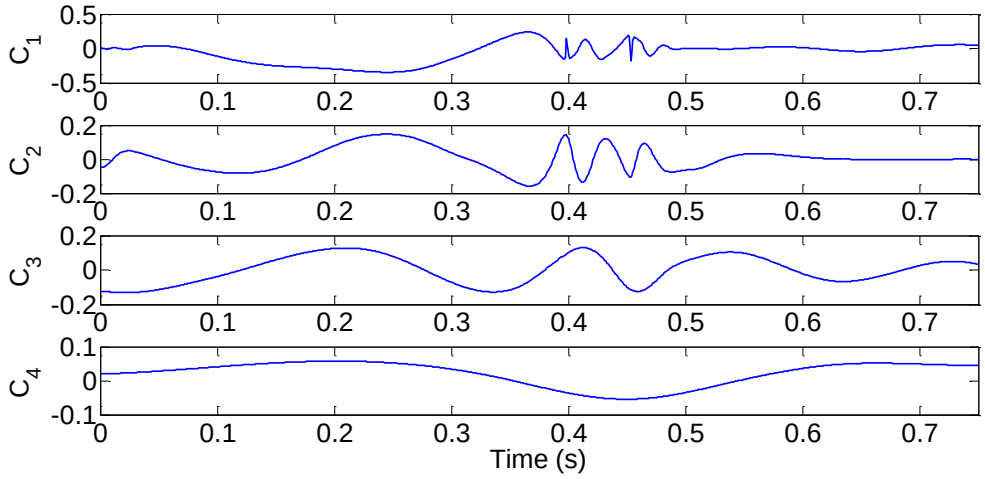

Fig. 7. IMFs by EMD of mid-span acceleration in forced vibration (Fig. 3(b)) for a beam with a localised elasto-plastic response at 9 m

A different problem to the one investigated here is identifying a weakened location (i.e., with a smaller stiffness than the rest of the bridge) that is already present in the structure before being excited and that remains constant during the test duration. The latter has been addressed by Meredith, et al. [18] using the EMD of the acceleration response to a moving load via the prior application of a moving average filter (MAF) to the original signal. The MAF acts as low-pass filter (set up to remove the bridge frequency) removing undesired high-frequency components but preserving a significant proportion of the static component of the response. The application of EMD to the filtered signal reveals a distinctive spike at the damaged location, and the time at which the spike occurs can be related to the position of the moving load to locate the damage (based on the vehicle speed and the time taken by the vehicle to reach the spike from the bridge support). However, limitations arise when trying to detect multiple damaged locations due to disruptions by filter transients, and similarly to wavelets, the algorithm is not as effective at detecting damage for higher speeds and noise levels.

2.2.3 EEMD

A noise-assisted data analysis method based on Wu and Huang [14], the so-called EEMD, is used to overcome the mode separating problem of EMD. EEMD defines the true IMF components as the mean of a prescribed ensemble number N_e of trials, where N_e is the number of times that white noise is added to the signal. The ensemble approach can separate the frequency naturally without any *a priori* subjective selection. Noise is introduced to the original data set, $x(t)$, as if a separate observation was indeed being made parallel to a physical experiment that could be repeated many times. Adding noise to the data provides a uniformly distributed reference frequency and IMFs associated to different series of noise uncorrelated with each other. The effect of EEMD decomposition is that the added white noise series cancel each other in the final mean of the corresponding IMFs. The EEMD process is illustrated in Fig. 8.

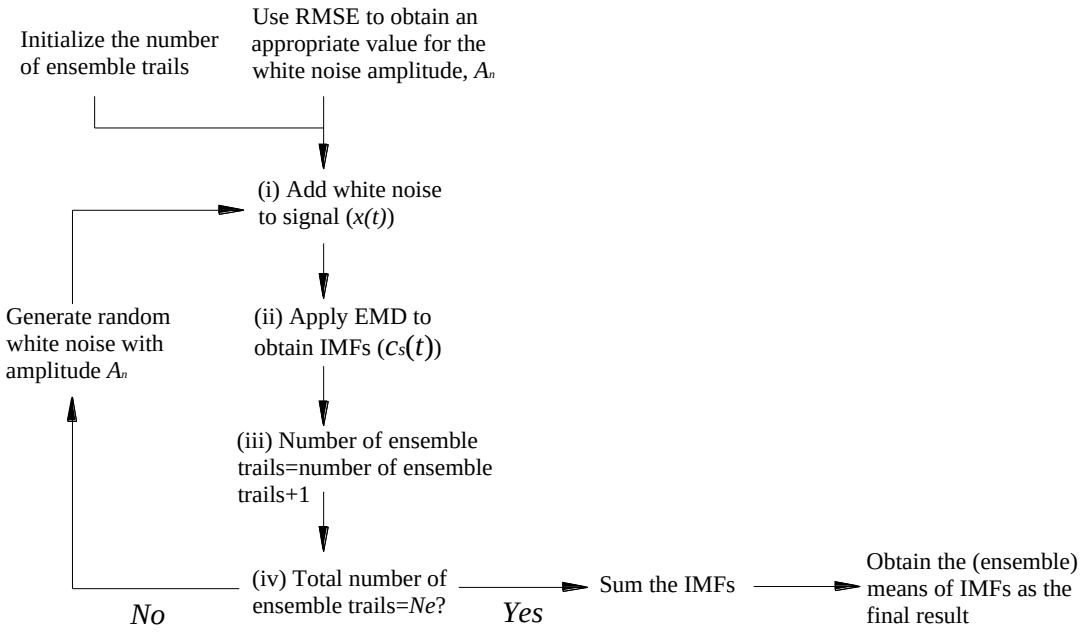

Fig. 8. Schematic of the EEMD process

Noise is added as $A_n\{N\}\sigma$ where A_n is noise amplitude, $\{N\}$ is a standard normal distribution vector with zero mean and unit standard deviation and σ is the standard deviation of the noise-free signal. The noise amplitude (A_n) greatly influences the performance of the EEMD method with regard to mode separation. On the one hand, too low of a noise amplitude will not introduce enough changes in the extremes of the decomposed signal and will have little effect on separating the signal completely. On the other hand, too high of a noise amplitude will result in redundant IMFs. If a signal is dominated by a high frequency component, white noise with low amplitude A_n is capable of separating the mixed modes easily. However, if the signal is dominated by low-frequency components, the amplitude of white noise A_n should be higher so that the mixed modes are separated. An index termed the relative root mean square error (*RMSE*) by Guo and Tse [38] is introduced to evaluate the performance of the EEMD at different noise amplitudes and to select an appropriate A_n value. In order to calculate *RMSE*, a number of IMFs ($c_1(t)$, $c_2(t)$...) is extracted by applying EEMD to the original signal with added noise (i.e., $x(t)$), and the IMF with the highest correlation coefficient between the IMF and the original signal ($x(t)$) is selected (i.e., $c_s(t)$). The correlation coefficient is established using the quality of a least squares fitting to the original signal $x(t)$. Then, $c_s(t)$ is used to calculate the relative *RMSE*, defined as the ratio between the root-mean-square of the error and the root-mean-square of the signal, where the error is the difference between the original signal ($x(t)$) and the selected IMF ($c_s(t)$) as in Equation (9).

$$\text{Relative } RMSE = \sqrt{\frac{\sum_{t=1}^{M}\left(x(t)-c_k(t)\right)^2}{\sum_{t=1}^{M}\left(x(t)-\overline{x}_0\right)^2}} \tag{9}$$

where M is the number of time samples of the signal, $c_s(t)$ is the k^{th} IMF chosen based on the highest correlation coefficient and $\overline{x}_0$ is the mean of the original signal $x(t)$. If the relative *RMSE* was very small or close to zero, it indicates that the chosen $c_s(t)$ is close to the original signal $x(t)$ with presence of white noise and the required decomposition process is not reached. If the relative *RMSE* value was high, the signal is separated from the noise and an adequate noise amplitude has been employed. Therefore, the value of A_n that maximizes the relative *RMSE* is selected to achieve the desired decomposition that will separate the

main signal from noise and other low-correlated components. Once the value of A_n to be used in the EEMD has been established, it is necessary to also prescribe N_e. Disregarding computational time, the higher the ensemble number N_e the lower the error. To some degree, continuing increasing N_e results in minor change in errors. N_e = 100 is found to be sufficiently accurate for the acceleration data under investigation and adopted here to optimize computational time [15].

Eight IMFs, shown in Fig. 9, are extracted ($c_1(t)$ to $c_8(t)$) when applying EEMD to the acceleration in Fig. 3(b). The computational time for simulating the acceleration response due to the moving load, programmed in MATLAB on a Windows 8.1 pro 2013 platform, is approximately 26 s with a i5-3230M CPU 2.6 GHz processor, 4.00 GB RAM and 64-bit operating system. The time that takes selecting the optimum noise amplitude (A_n) in the iterative RMSE process and obtaining the corresponding IMFs is approximately 180 s. The total computational time in producing Fig. 9 is 180 + 26 = 206 s. $c_1(t)$ and $c_2(t)$ show the higher frequency components of the acceleration signal attributed to noise and elasto-plastic response. The time interval at which the element responds in an elasto-plastic manner is visualized by spikes at 0.39 s and 0.45 s followed by a response (and stiffness) returning to normal (i.e., approximately a flat straight line) in agreement with Fig. 4. IMFs $c_3(t)$ and $c_4(t)$ also show spikes at instants of loss in stiffness although they are not as sharp as in $c_1(t)$ and $c_2(t)$. $c_5(t)$ and $c_6(t)$ contain low frequency components already observed for the perfectly linear ('healthy') beam. The remaining IMFs ($c_7(t)$ and $c_8(t)$) do not represent any frequency associated to the dynamic oscillations of the beam, but signal content related to the static component of the response.

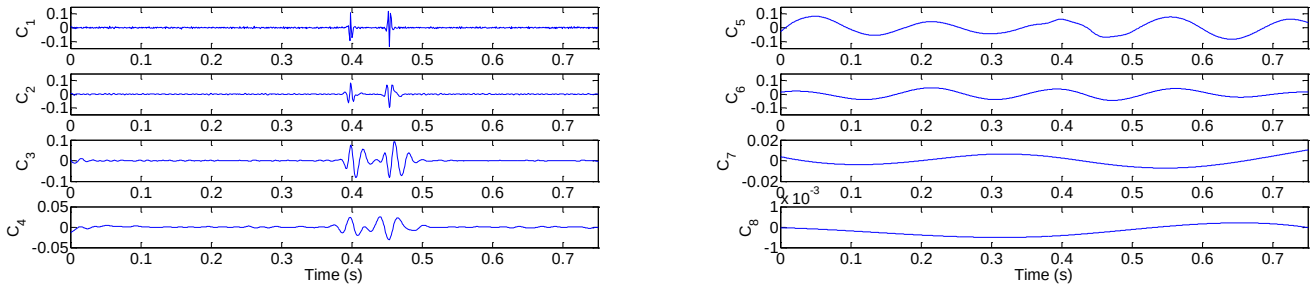

Fig. 9. IMFs by EEMD of mid-span acceleration in forced vibration (Fig. 3(b)) for a beam with a localised elasto-plastic response at 9 m

Fig. 10 shows the PSDs of $c_5(t)$ and $c_6(t)$ leading to frequencies of 5.9 Hz (near the exact 5.8 Hz of the perfectly linear elastic beam) and 5.5 Hz (below the frequency of the elasto-plastic beam which is 5.71 Hz) respectively. It is worth mentioning that, in a practical situation, the location of the first bridge eigenfrequency depends on the characteristics of the signal and noise level, and it must not be necessarily found in $c_5(t)$ and $c_6(t)$. The EEMD utilizes its frequency separation capability of the EMD to become a truly dyadic filter bank (decomposing a broadband signal into a collection of sub-bands with smaller bandwidths and slower sample rates) for any data. By adding prescribed noise amplitude, the EEMD alleviates the problem of mode mixing and preserves the physical meaning of the decomposition to a large degree, although complete settlement of the mode mixing problem is still out of reach.

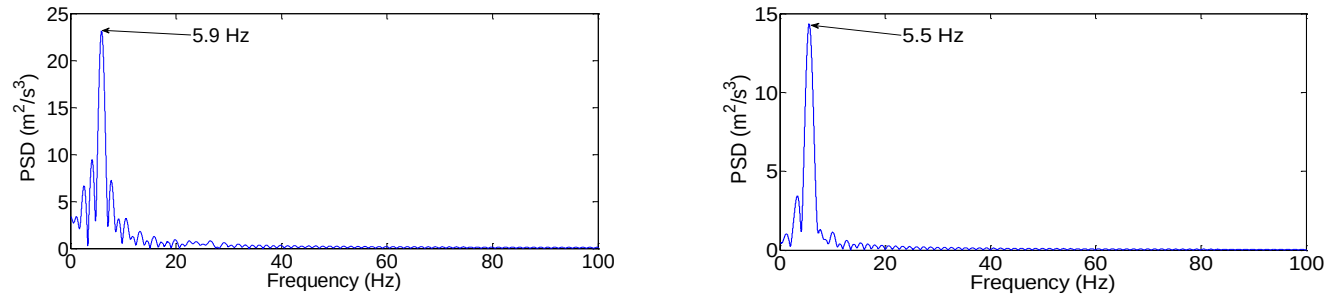

(a) (b)

Fig. 10. PSD of (a) IMF5 and (b) IMF6

This section has been an illustration of how EEMD can be used to locate the changes in stiffness at 0.39 s and 0.45 s. Two distinctive spikes have stood out at the lowest IMF where other 'healthy' components have been successfully extracted. EEMD has outperformed wavelet analysis and EMD for the beam response under investigation. At this point, it is important to reiterate that the simulated response has been produced using a simple moving constant load model where no VBI or added contamination has been considered in the theoretical acceleration response. These figures have been used only to demonstrate the basic principles behind the detection of nonlinear response using EEMD, i.e., that a distinctive spike will appear in problems where the mechanical properties of the structure are altered at some instant during the test. Therefore, the remaining of the paper focus on identifying an elasto-plastic response from EEMD of the acceleration response in more challenging scenarios with influence from the road profile, VBI, noise and different measurement locations and sizes of the region affected by the bilinear hysteretic model with respect to the travelling path of the vehicle.

3. Application of EEMD to detection of stiffness changes using the acceleration response of a plate to a moving sprung 2-axle vehicle model

The same rationale employed in Section 2 is applied here. The VBI system used to simulate accelerations is explained first, and a discussion of the results by EEMD in multiple scenarios follows.

3.1 Vehicle-Bridge interaction simulation model

FEM has been extensively used in the past to numerically approximate the response of a VBI system [1, 39-41]. The bridge deck (Section 3.1.1) is discretized into 2-D plate elements with a bi-linear moment curvature relationship at selected locations. The vehicle (Section 3.1.2) is modelled as a series of unsprung and sprung lumped masses interconnected by spring-dampers. The interaction between both systems can be solved using a coupled [23] or uncoupled [41-43] approach. In most of cases both approaches are equivalent, therefore, the uncoupled approach is chosen here (Section 3.1.4) on the basis of computational efficiency.

3.1.1 Bridge model

The bridge is modelled as simply supported orthotropic thin plate and is based on Kirchhoff's plate theory [25, 44]. The deck is discretised into 30 elements in the x-direction and 24 elements in the y-direction (i.e., each plate element is 0.5x0.5m with a thickness of 0.8 m) as shown by Fig 11. Each plate element is defined by 4 nodes and a total of 16 DOFs, namely vertical displacement, rotation in the x-direction, rotation in y-direction and nodal twist (which takes into account the discontinuity in the slope along the edge of the elements [42]) in the x-y direction at all nodes. This element differs from Kirchhoff's plate elements which ignore the nodal twist DOFs and consist of a total of 9 DOFs. The bridge has the same dimensions as in Section 2 (15x12x0.8 m) and it is assumed to be orthotropic with Young's modulus in the longitudinal and transverse directions assumed to be 31×10^9 N/m^2 and 14×10^9 N/m^2 respectively. Poisson's ratio, unit weight and damping ratio are taken as 0.15, 1200 kg/m^3 and 2% [23, 24] respectively. For the original properties in the elastic range, the main modes of vibration of the bridge have natural frequencies of 8.23 (longitudinal), 17.1 (torsional) and 32.88 (longitudinal) Hz. Unless otherwise specified, the plate elements that will experience a change in stiffness are assumed to be located at 9 m from the left support and they stretch along the width of the bridge.

Acceleration signals are simulated at mid-span as in the previous section, with a scanning frequency of 1000 Hz, which is within the operative range of modern accelerometers. A high scanning frequency does not necessarily improve resolution but can be beneficial in dealing with signals corrupted with noise. The bi-linear hysteretic moment-curvature formulation used for a beam element in Section 2.1 is expanded to plate elements in Appendix A and applied to selected elements in the deck model. Acceleration data is obtained at 25 locations across the mid-span section (i.e., for a longitudinal coordinate of 7.5 m) corresponding to the vertical displacement DOF of each node.

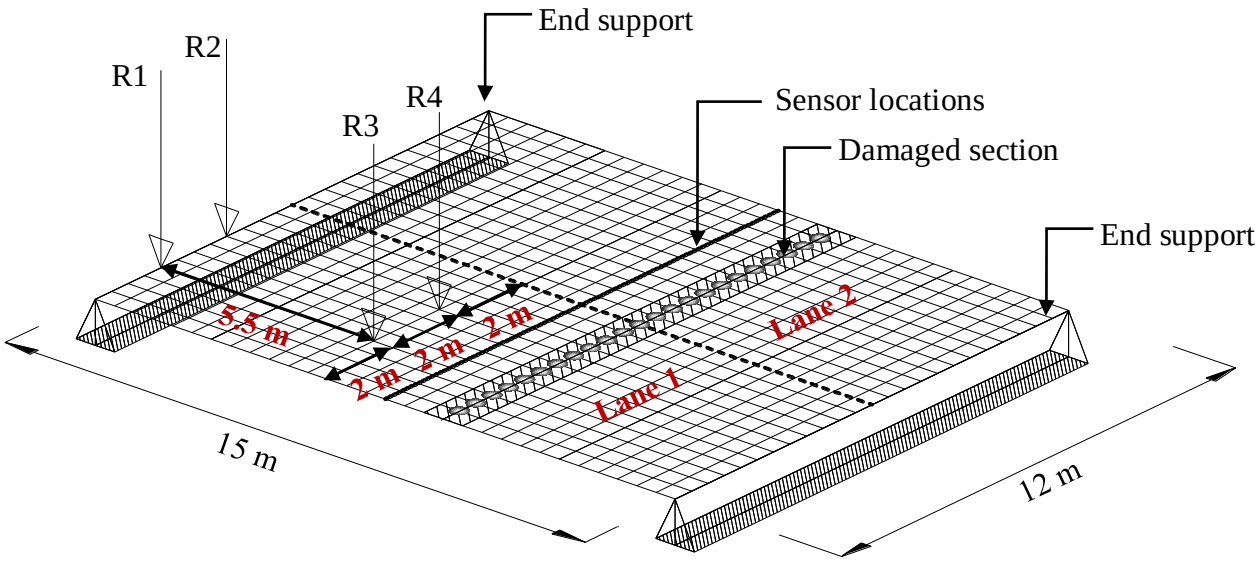

Fig. 11. Simply supported bridge FEM

The general equation of motion for a bridge under a moving load is given by:

$$[M]_b \{\ddot{u}_b(t)\} + [C]_b \{\dot{u}_b(t)\} + [K]_b \{u_b(t)\} = \{F_b(t)\} \tag{10}$$

where $[M]_b$, $[C]_b$ and $[K]_b$ are the bridge mass, damping and stiffness matrices respectively, $\{F_b(t)\}$ is the external force exerted on the DOFs of the bridge (N), and $\{\ddot{u}_b(t)\}$, $\{\dot{u}_b(t)\}$ and $\{u_b(t)\}$ are the acceleration (m/s^2), velocity (m/s) and displacement (m) respectively at each DOF and time t.

3.1.2 Vehicle model

A 2-axle 3-D vehicle is modelled with axles represented as rigid bars connecting lumped masses at both ends corresponding to the mass of the wheel and suspension. Axle spacing is 5.5 m [45] and the wheelbase distance is 2 m (Fig. 12). The vehicle path within the bridge is 2 m from the right edge of the deck as shown in Fig. 11. Fig. 12 illustrates the vertical displacement, v, and rotational DOFs, θ_x and θ_y, of the sprung mass. The vertical displacements of the front right, front left, rear right and rear left un-sprung masses are denoted by $v_{u,fr}$, $v_{u,fl}$, $v_{u,rr}$ and $v_{u,rl}$ respectively.

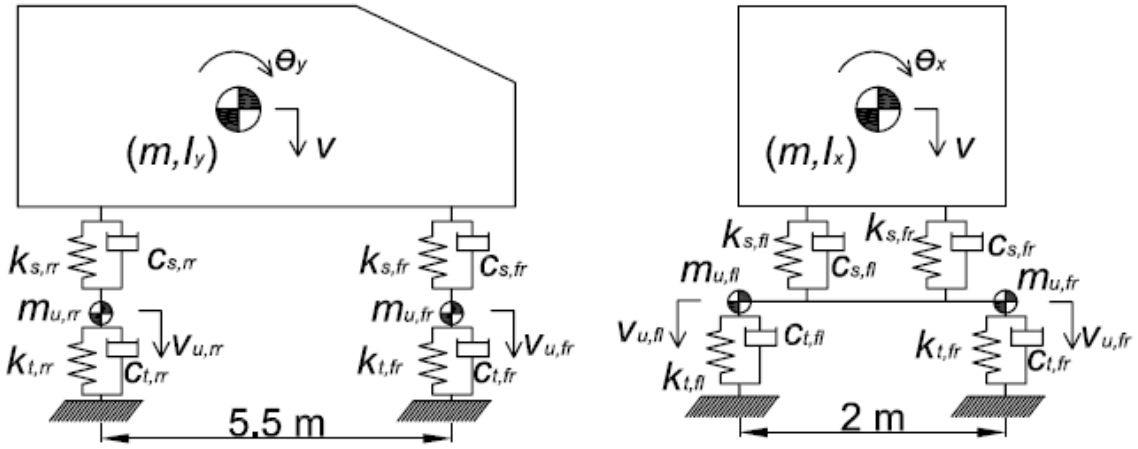

(a) (b)

Fig. 12. Schematic illustration of the vehicle model: (a) Right side view and (b) Front view

The centre of the body mass is located at the centre of the vehicle (i.e., it is equidistant from the four wheels). It is assumed that the values of vehicle tyres and suspensions' stiffness and viscous damping are the same for all wheels and axles. The mechanical properties of the vehicle are based on values available in the literature [42, 46, 47] and given in Table 1.

Table 1: Vehicle properties (where second subscript '*f*' and '*r*' stand for front and rear axles respectively, and third subscript '*l*' and '*r*' refer to left and right sides of the axle respectively)

	Value	Symbol in Fig. 12
Sprung mass (kg)	16.5×10^3	m
Un-sprung mass (kg)	375	$m_{u,fr}, m_{u,fl}, m_{u,rr}, m_{u,rl}$
Mass moment of inertia (kg·m^2)	425×10^3	I_x
	425×10^3	I_y
Suspension stiffness (N/m)	1×10^6	$k_{s,fr}, k_{s,fl}, k_{s,rr}, k_{s,rl}$
Suspension damping (N·s/m)	5×10^3	$c_{s,fr}, c_{s,fl}, c_{s,rr}, c_{s,rl}$
Tyre stiffness (N/m)	1×10^6	$k_{t,fr}, k_{t,fl}, k_{t,rr}, k_{t,rl}$
Tyre damping (N·s/m)	3×10^3	$c_{t,fr}, c_{t,fl}, c_{t,rr}, c_{t,rl}$
Suspension offset (m)	0	d

The dynamic forces of the vehicle are obtained by imposing the equilibrium of forces and moments acting on the vehicle and expressing them in terms of their DOFs [41, 46, 47]. The equation of motion of the vehicle dynamic system is given by:

$$[M]_v \{\ddot{v}_v(t)\} + [C]_v \{\dot{v}_v(t)\} + [K]_v \{v_v(t)\} = F_v(t) \tag{11}$$

where $[M]_v$, $[C]_v$ and $[K]_v$ are the global mass, damping and stiffness matrices of the vehicle respectively, $F_v(t)$ is the force at the contact point with the road profile (N), and $\ddot{v}_v$, $\dot{v}_v$ and v_v are the accelerations (m/s^2), velocities (m/s) and displacements (m) respectively of the vehicle DOFs.

3.1.3 Road profile

The height of road profile irregularities, $r(x)$, for a single track can be generated from PSDs as a random stochastic process using an inverse fast Fourier transform method or adding sinusoids as in:

$$r(x) = \sum_{i=1}^{W} \sqrt{2G(n_k)\Delta n}\cos(2\pi n_k x - \theta_i) \tag{12}$$

where $G(n_k)$ is the PSD function in m^2/cycle/m; n_k is the wave number (cycle/m); θ_i is a random number uniformly distributed from 0 to 2π; Δn is the frequency interval ('$\Delta n = (n_{max} - n_{min}) / W$' where n_{max} and n_{min} are the upper and lower cut-off frequencies respectively); W is the total number of waves used to construct the road surface and x is the longitudinal location for which the road height is being sought. $G(n_k)$ is determined by $a/(2\pi n_k)^2$ according to ISO [48] where a (m^3/cycle) is the roughness coefficient, which is related to the amplitude of the road irregularities. Road classes vary from smooth (class 'A' with a low roughness coefficient) to very poor (class 'E' with a high roughness coefficient) [48]. In particular, roughness coefficients a of 4×10^{-6}, 96×10^{-6}, and 1536×10^{-6} m^3/cycle have been adopted for road classes 'A', 'C' and 'E' respectively. The approach length prior to the bridge has significant implications on the response of the vehicle and hence, the response of the bridge. An approach length of 150 m has been adopted in the investigation and possible expansion joints or potholes have not been considered.

The 3D vehicle model has left- and right-hand wheel tracks, and thus, it requires two input profiles. One of the tracks can be generated by applying random phase angles θ_i to Equation (12) for a given PSD. When calculating the second track, it must be noted that it is statistically related to the first track via a coherence function. Coherence functions vary between 0 (totally uncorrelated) and 1 (perfectly correlated) and they have the purpose of guaranteeing good and poor correlation between two parallel tracks for long and short wavelengths respectively. If an isotropic and homogeneous road surface is assumed (i.e., same PSD for both tracks), then, the coherence function will vary with wave number n_k as in Equation (13):

$$coh_{lr}(n_k) = \frac{|G_{lr}(n_k)|}{G(n_k)} \tag{13}$$

where $G_{lr}(n_k)$ and $G(n_k)$ are the cross-spectral and direct spectral densities of the individual tracks respectively.

Taking into account the aforementioned, an isotropic correlated road surface is generated using the inverse Fourier transform method proposed by Cebon and Newland [49]. In VBI studies, it is normally assumed that the road and vehicle make contact at a single point which ignores the width of the tyre. Therefore, a MAF with a length corresponding to the width of the tyre (0.24 cm is used here) is applied to the randomly generated road profile in order to simulate the effect of a tyre [50, 51]. An example of road class 'A' surface with a geometric spatial mean of 4×10^{-6} m^3/cycle resulting from this process is shown in Fig. 13. In the simulations that follow, the irregularities of the left- and right-hand wheel tracks are selected from this carpet unless otherwise specified.

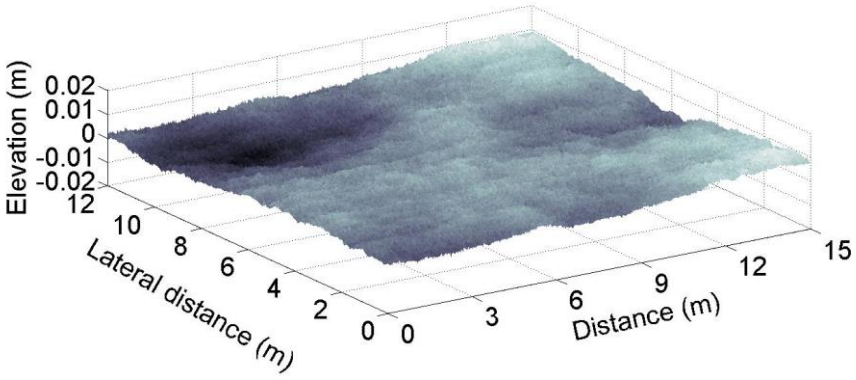

Fig. 13. Example of class 'A' road profile over the bridge after applying the moving average filter

3.1.4 Interaction between vehicle and bridge systems

VBI is solved based on an uncoupled iterative system [41, 42] with small changes to incorporate the nonlinear elementary stiffness matrixes of Appendix A at selected locations. The process is as follows:

(a) The vehicle vertical forces ($F_v(t)$) due to the road profile only are obtained using Equation (11).
(b) The displacement ($u_b(t)$) and bending moment ($M_n(t)$) of the bridge under each tyre due to dynamic loads ($F_v(t)$) in (a) is obtained applying Equation (10).
(c) If the bending moment ($M_n(t)$) exceeds the yield bending moment (M_p), the nonlinear stiffness matrix of the plate is introduced at selected DOFs. Otherwise, the existing linear stiffness matrix [K_b] is employed.
(d) The displacement response ($u_b(t)$) is added to the road profile ($r(t)$).
(e) The vertical forces due to a new profile ($u_b(t)+ r(t)$) are obtained using Equation (11).
(f) Steps (b) to (e) are repeated until a tolerance value is reached. Here, the tolerance value is defined by the difference between consecutive values of the maximum bending moment in the plate being less than 0.1%. This value is a stoppage criteria in which the difference between consecutive maximum bending moments becomes negligible, i.e. tolerance > (max bending moment at time 't')-(max. bending moment at the preceding time 't-Δt')/ (max bending moment at time 't') ×100.

The iterative process above has advantages over a coupled solution because of its efficiency and flexibility that allows modelling and solving bridge and vehicle responses separately (i.e., using the Wilson-θ integration method in these simulations). The results match solutions provided by Cantero, et al. [42] and Dowling, et al. [52].

3.2 Calibration of EEMD parameters and application to identification of changes in stiffness

Section 2.2.3 has demonstrated the improvement in detecting a sudden stiffness change when using the EEMD method over the conventional EMD method for a beam under moving point load, mostly due to the reduction of the mode mixing problem. Two aspects of the EEMD to be addressed prior to its implementation are the noise amplitude (A_n) and number of ensemble trails (N_e). These values are going to depend on the simulated signal. For instance, Fig. 14 plots the relative *RMSE* (using Equation (9)) against noise amplitude for different levels of post-yield stiffness loss in the simulated signal (i.e., different p values in Fig. 2(b) at the damaged location shown in Fig. 11). From Fig. 14, the most appropriate value of noise amplitude (i.e., maximizing relative *RMSE*) would be around 0.55 for post-yield stiffness losses of 0% (p = 1), 10% (p = 0.9) and 50% (p = 0.5), and 1.85 for a post-yield stiffness loss of 30% (p = 0.7). The ensemble number N_e is fixed at 100.

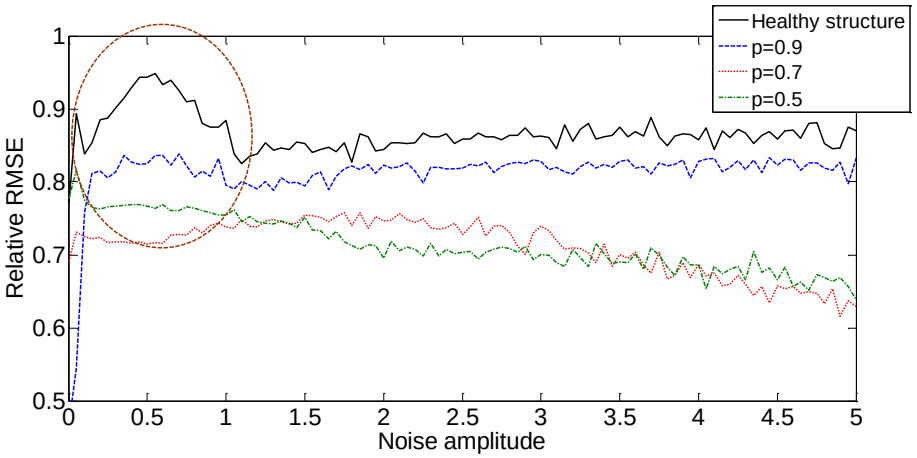

Fig. 14. Relative *RMSE* versus noise amplitude for different levels of post-yield stiffness loss

The first natural frequencies of the bridge for the short time period when selected elements are in the elasto-plastic range will vary for different p values or stiffness loses. In the 15 m long plate model with the elasto-plastic region at 9 m under investigation, these frequencies are 8.23, 8.21, 8.18 and 8.13 Hz for 0%, 10%, 30% and 50% stiffness losses respectively. For p = 0.51, the first frequencies of the plate (which are 8.23, 17.1 and 32.88 Hz for the 'healthy' state, i.e., p = 1) become 8.13, 17.05 and 32.39 Hz for the short time window when selected elements enter the elasto-plastic range. Fig. 15 shows the acceleration signal of the bridge at mid-span for lane 1 where the vehicle is travelling (at 3 m from bridge centreline) in time and frequency domains. The first (8.03 Hz) and second (17.3 Hz) natural frequencies can be visualized in the PSD of Fig. 15(b), although there are small differences with the true values due to the partial elasto-plastic response and time resolution.

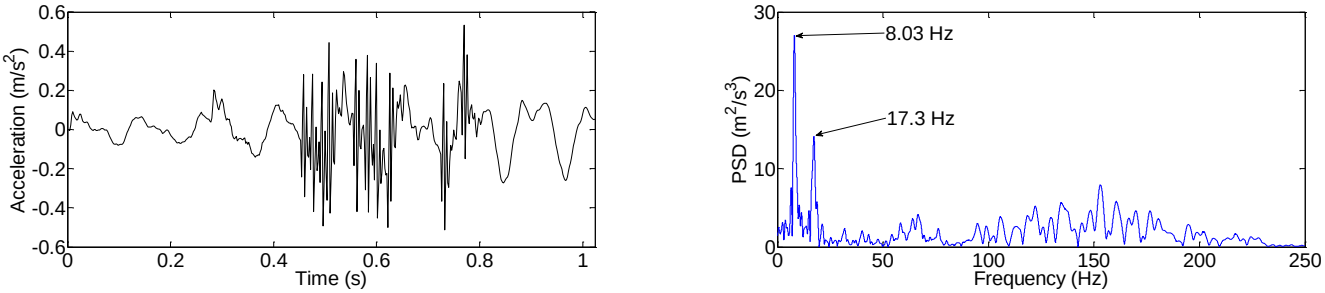

(a) (b)

Fig. 15. Mid-span acceleration response (at 3 m from bridge centreline in lane 1) versus time of a bridge with an elasto-plastic region with p = 0.51 at 9 m: (a) time domain; (b) frequency domain

Fig. 16 shows the true time instances at which all the transverse elements at 9 m from the left support experience a change in longitudinal stiffness: 0.45-0.5 s, 0.55-0.62 s and 0.72-0.76 s. Stiffness ratio is defined as the actual stiffness divided by the stiffness in the elastic range. There are no changes in the transverse stiffness. 1st and 2nd axle loads will reach the elasto-plastic region at 0.45 s (= 9/20) and 0.72 s (= 14.4/20) respectively and these time intervals approximately cover the period when the vehicle travels over the region. The acceleration in Fig. 15(a) reflects this elasto-plastic response by a noticeable increase in amplitude after 0.45 s, however, it is unclear at what time instance this drop in stiffness returns to the original value or when it drops again.

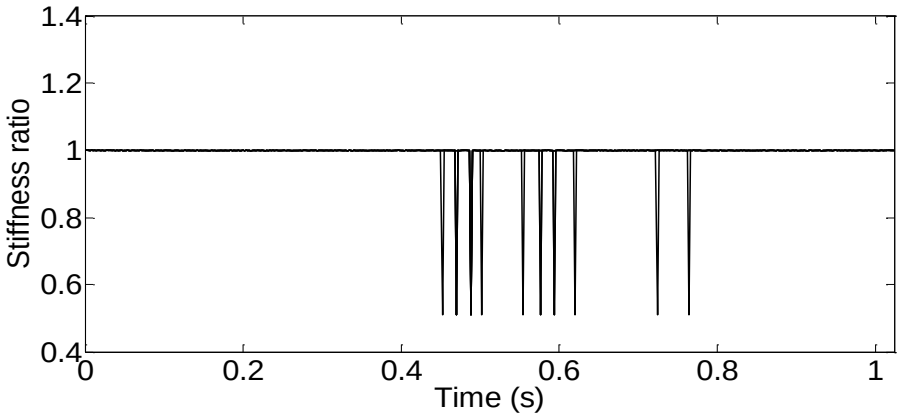

Fig. 16. Variation of longitudinal stiffness ratio of elements at 9 m from left support with time

The EEMD method is applied to the acceleration signal of Fig. 15(a) and the resulting IMFs ($c_1(t)$ to $c_8(t)$) are plotted in Fig. 17. The first IMFs ($c_1(t)$ to $c_3(t)$) extract the higher frequency components of the signal associated with noise and elasto-plastic periods. In the first IMF ($c_1(t)$), the jumps in amplitude between 0.45-0.5 s, 0.55-0.62 s and 0.7-0.76 s are associated with the stiffness drops shown in Fig. 16 at similar time instances. These stiffness drops are not as clear in IMFs $c_2(t)$ and $c_3(t)$ where high frequency components of the VBI system are also captured.

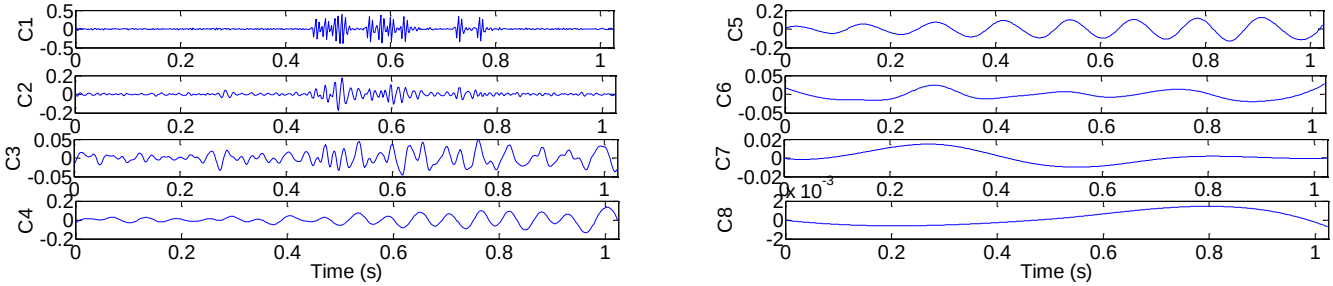

Fig. 17. IMFs by EEMD of mid-span acceleration response (3 m from bridge centreline in lane 1) in the case of a structure with a localised elasto-plastic response with p = 0.51 at 9 m

Fig. 18 shows the IMF1 from Fig. 17 together with the stiffness variation from Fig. 16, to highlight how accurately the spikes in IMF1 correspond to instant changes in stiffness.

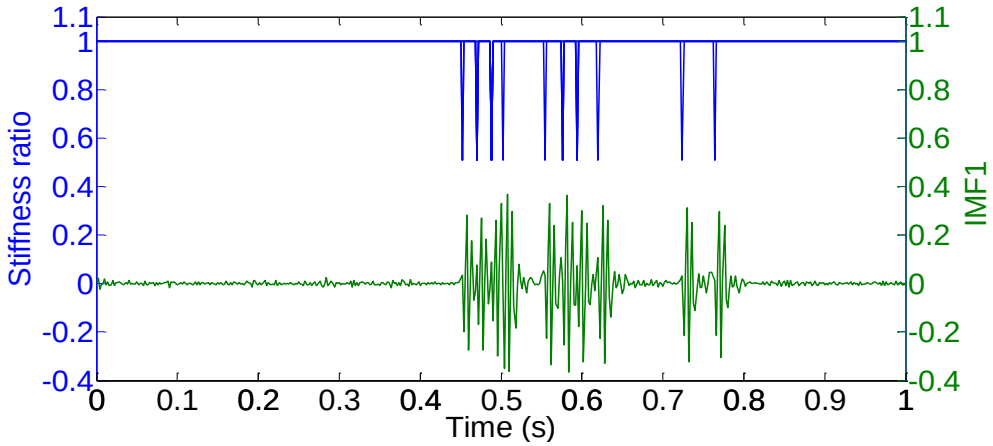

Fig. 18. Comparison of stiffness ratio and IMF1 of elements at 9 m from left support versus time

Fig. 19(a) shows the PSD associated to IMF4 ($c_4(t)$) with two peaks at 8.3 Hz and 17.3 Hz in good agreement with the first two natural frequencies of the 'healthy' state of the bridge. Fig. 19(b) shows the PSD associated to IMF5 ($c_5(t)$) which extracts the first frequency, with a lower value than that of elasto-plastic range (8.13 Hz). These results are similar to those experienced for the 1-D beam model in Section 2.2.3, which suggest that some aspects of mode mixing still exist in the decomposition process, although to a smaller extent than that observed in the EMD method. Higher IMFs ($c_6(t)$ to $c_8(t)$) are residues that are mostly attributed to static content of the response.

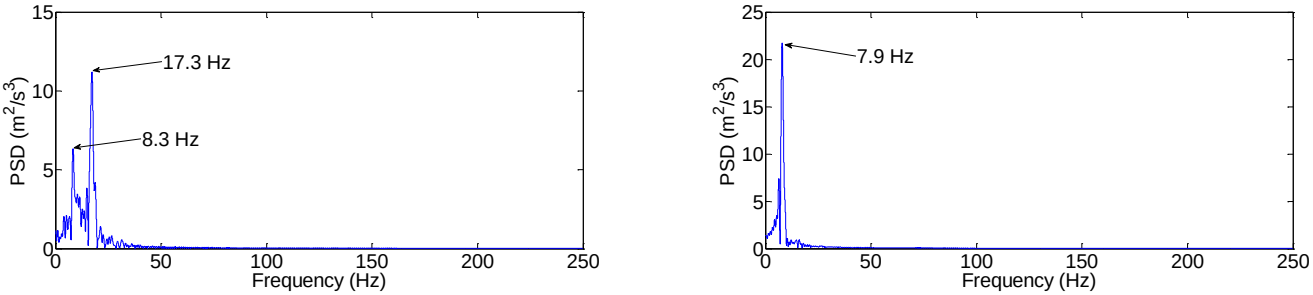

(a) (b)

Fig. 19. PSD of: (a) IMF4 and (b) IMF5 from Fig. 17

This section has demonstrated the effectiveness of EEMD in separating higher frequency components associated to the added white noise and the elasto-plastic response from the natural frequencies of the bridge, a major issue in other signal processing techniques reviewed in Section 2. This is highlighted by the spikes that stand out in IMF1 ($c_1(t)$) which correspond to instant changes in stiffness and which are not significantly interfered by any other frequency components of the acceleration signal. Therefore, if it was possible to identify the entrance and speed of the vehicle on the bridge (i.e., via a weigh-in-motion system installed prior to the bridge), damage can be located approximately using the approach suggested by Meredith, et al. [18], i.e., multiplying the vehicle speed (20 m/s) by the time between the vehicle entrance and the first spike (20 x 0.45 = 9 m, which is the longitudinal location of the section experiencing elasto-plastic changes). In the following sections, the impact of the number of selected elements across the transverse (y) direction experiencing an elasto-plastic response, road profile, vehicle speed and noise on the identification of spikes in IMF1 is discussed.

3.3 Impact of extent of elements undergoing an elasto-plastic response

Fig. 20(a) shows IMF1s ($c_1(t)$) for a 'healthy' bridge (all plate elements with p = 1) in 3-D in which the x-axis is time (s), and the y- and z-axes are measurement location and amplitude of each IMF1 respectively across the bridge width. In these 3D plots, acceleration responses are calculated every 0.5 m along the y-direction of the bridge mid-span section and for each of them, an IMF is calculated using EEMD and represented in the figure. Fig. 20(b) shows sections through: A-A) acceleration at a quarter (3 m from the bridge edge in lane 1 where vehicle is travelling), B-B) middle (at the bridge centreline) and C-C) three-quarter (9 m from the bridge edge in lane 1) of bridge width. The purpose of the three sections is to show the influence of the load position with respect to the location of the accelerometer on the identification of spikes indicative of having exceeded the yielding point. It can be seen that for a 'healthy' plate deck (p = 1 in all elements), the amplitudes of the IMF1s in Fig. 20 are relatively smooth in contrast to cases that will presented further on with p = 0.51.

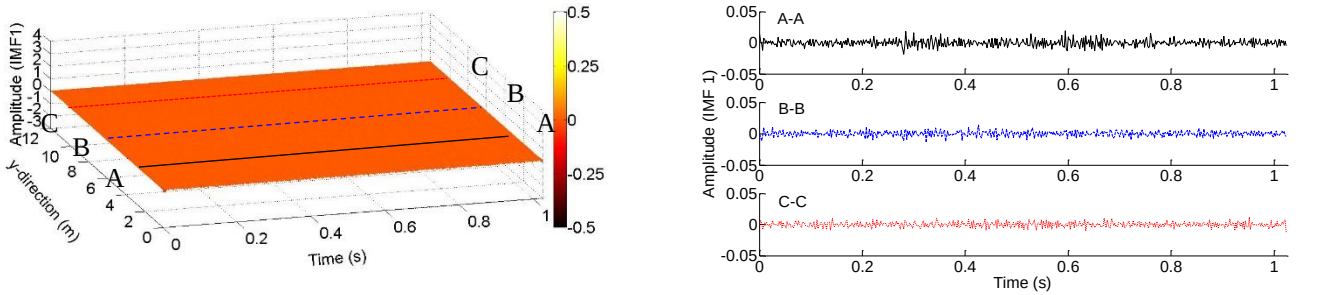

(a) (b)

Fig. 20. IMF1s of accelerations at mid-span for perfectly elastic response in all plate elements: (a) IMF1 amplitude versus time across the bridge width, (b) IMF1s for three mid-span acceleration locations

In the Section 3.2, all plate elements at 9 m from the left support (i.e., across the entire 12 m width) have been assumed to respond following the bilinear hysteretic model defined in Appendix A. However, the extent of elements affected by an elasto-plastic response can have profound implications on its identification. In this section, the regions shown in Fig. 21 are investigated. 'Case 1' assumes that the elasto-plastic elements span the full width (0.5x12 m) of the bridge (as in Section 3.2), 'Case 2' spans half the bridge width (0.5x6 m) and 'Case 3' is localised around one element (0.5x0.5 m).

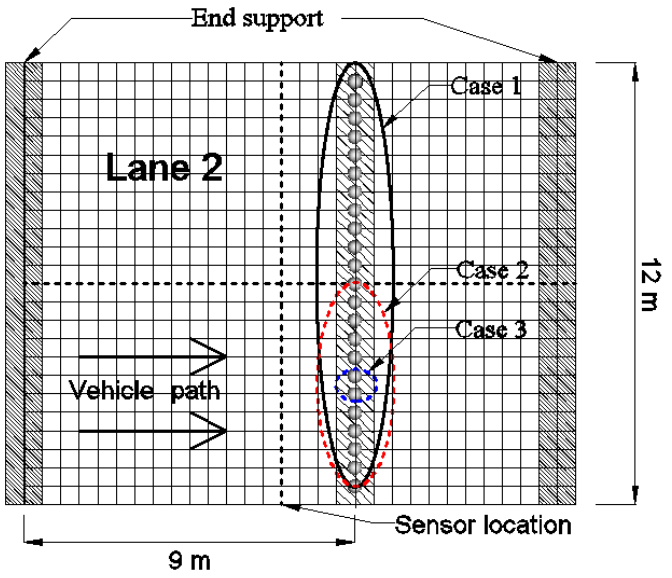

Fig. 21. Plan view of bridge with three cases of elasto-plastic regions

Fig. 22 shows the results of IMF1 of accelerations across the width of the bridge for the three cases of Fig. 21. The true longitudinal stiffness ratio is plotted against time in Fig. 22 (a) for 'Case 1' for all elements at 9 m from left support. The transverse stiffness remains constant throughout the time that the load is on the bridge. This figure is used as reference to validate the local 'spikes' identified in IMF1 truly correspond to stiffness changes. The spikes with highest amplitude in Figs. 21(b) and (c) closely resemble the stiffness changes in Fig. 22(a) at time intervals 0.45-0.5 s, 0.55-0.62 s, and 0.72-0.76 s. Fig. 22(c) analyse the same three acceleration locations of Fig. 20(b) with a perfectly elastic response, but here peaks are more distinctive. Comparing the three measurement locations in Fig. 22(c), it can be seen that the spikes are more significant as the location of the simulated response gets closer to the path of the load as a result of higher load concentration and load effects. Nevertheless, all three acceleration locations in Fig. 22(c) are able to perceive the stiffness changes for 'Case 1' successfully.

Fig. 22(d-f) show the equivalent graphs for 'Case 2'. Fig. 22(e) illustrates that the elasto-plastic region is noticed by acceleration locations in the same lane where the region is defined. The spikes are identifiable in the two of the three sections of Fig. 22(f) for time instances of 0.45-0.5 s, 0.55-0.62 s, and 0.7-0.78 s in which a drop in stiffness occur in the elasto-plastic region. It can be seen how the amplitude of the spikes

reduces as the acceleration location moves away from the travelling load of the path and from the elasto-plastic region.

'Case 3' (Figs. 22(g) to (i)) is obviously more difficult to detect than previous cases. Certainly, small 'spikes' in the amplitude of IMF1 at the instant of exceeding the linear elastic limit are observed around times of 0.55 s and 0.75 s in section A-A (Fig. 22(i)) which echo those provided by Fig. 22(g), although the magnitude of the IMF1 coefficients in 'Case 1' are about one tenth smaller than seen before. The mid-span acceleration corresponding to location B-B shows smaller amplitudes than A-A at times of 0.55 s and 0.75 s and therefore, they are masked by other spikes of similar magnitude that were already seen in the IMF1 of the perfectly elastic plate model of Fig. 20(b). When increasing the distance between the elasto-plastic element and the measurement point, the stiffness loss goes unnoticed to the response as shown by section C-C.

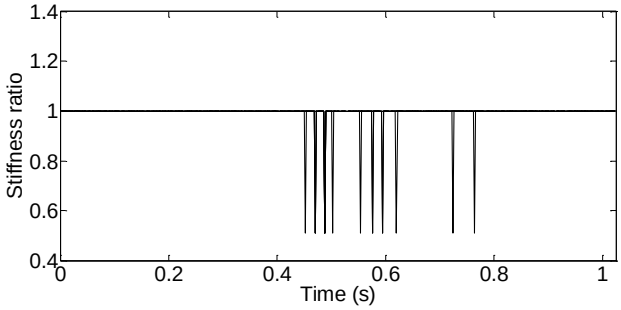

(a)

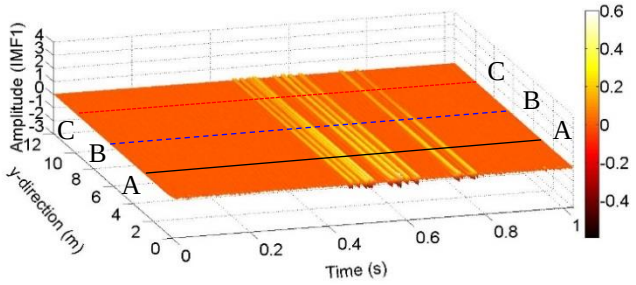

(b)

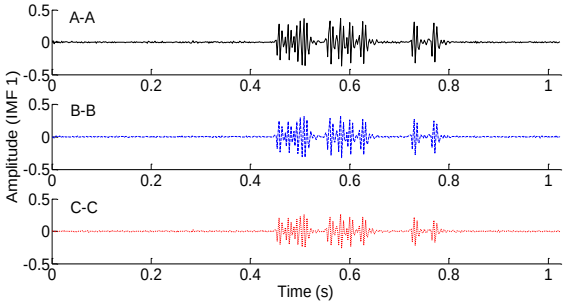

(c)

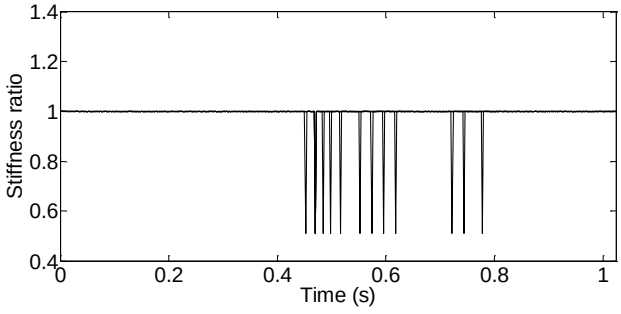

(d)

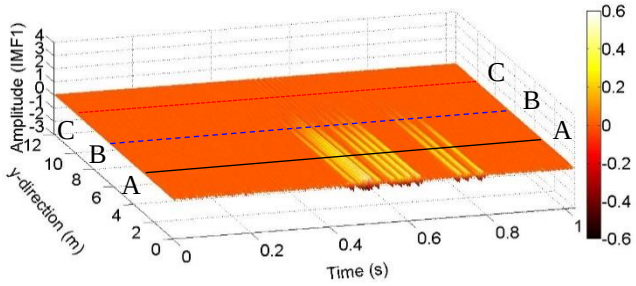

(e)

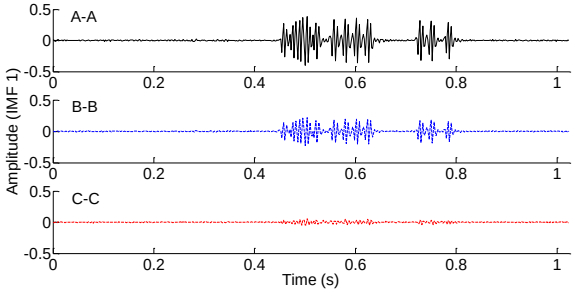

(f)

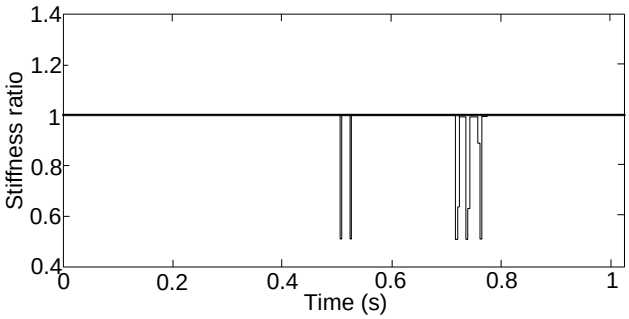

(g)

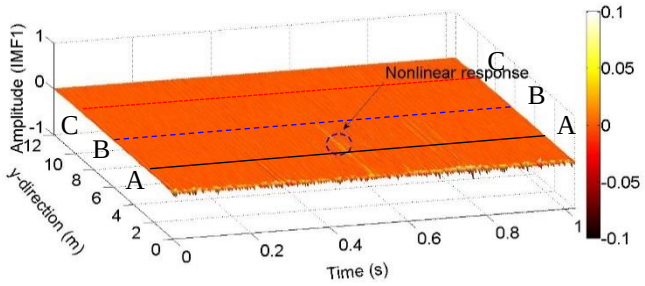

(h)

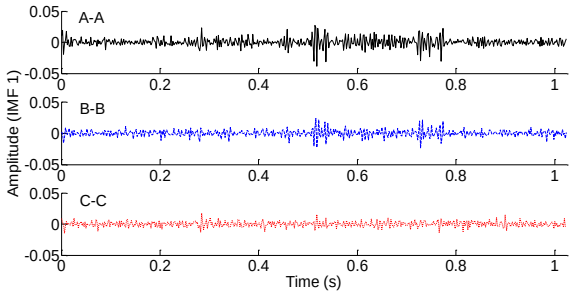

(i)

Fig. 22. IMF1s using EEMD of accelerations at mid-span for a plate model with three elasto-plastic regions at 9 m: (a) True variation of longitudinal stiffness ratio at elements along the width of the bridge at 9 m from left support with time for 'Case 1', (b) IMF1 amplitude versus time across the bridge width for 'Case 1', (c) Three sections across (b), (d) True variation of longitudinal stiffness ratio at elements for 'Case 2' at 9 m from left support with time, (e) IMF1 amplitude versus time across the bridge width for 'Case 2', (f) Three sections across (e), (g) True variation of longitudinal stiffness ratio at elements for 'Case 3' at 9 m from left support with time, (h) IMF1 amplitude versus time across the bridge width for 'Case 3', (i) Three sections across (h)

The sudden and close changes in stiffness observed in Figs. 22(a), (d) and (g) are caused by the short time intervals in which the structure exceeds the yield limit. Once the yield limit is exceeded, the stiffness will return relatively quickly to its original elastic value at unloading. Bridge elements are exposed to waves of cyclic loading and unloading due to the oscillatory nature of the dynamic component of the bridge response. The latter derives in sudden drops of stiffness and rises to an original value in those elements experiencing an elasto-plastic response which tends to lead to concentration of spikes in the IMF1s.

3.4 Impact of Road Profile

Road irregularities produce excitations in the vehicle that will affect the bridge response, in particular, its high frequency content will have repercussions on the lowest IMFs where the elasto-plastic response is identified. A road class 'A' has been used in simulations for the results of Sections 3.2 and 3.3. Two rougher road classes 'C' (average) and 'E' (very poor) are defined according to ISO as in Section 3.1.3 and used in the simulations. The patterns of stiffness changes for class 'A' (Fig. 22(a)), 'C' (Fig. 23(a)) and 'E' (Fig. 23(d)) are significantly different. Rougher road profiles induce larger vehicle dynamic forces and larger load effects and an earlier stiffness change at the elasto-plastic elements. Fig. 23(a) shows stiffness changes at approximately 0.4 s and 0.5 s that are resembled by Figs. 23(b) and (c). Similarly to Fig. 22(c) for a class 'A' profile, the maximum amplitude in Fig. 23(c) for a class 'C' occurs at lane 1 where the vehicle is travelling. In Fig. 23(c), amplitudes of 0.4 and 0.243 for the spike at 0.43 s are obtained in sections A-A and B-B respectively. For class 'E' (Figs. 23(d), (e) and (f)), the road irregularities produce multiple stiffness changes and as a result, many amplitude variations in the IMF, even after 0.7 s. The spikes in the IMF

distinguish perfectly elastic periods (before 0.3 s and around 0.6 s) from elasto-plastic periods for most of the signal duration, except towards the end (the 2nd axle will leave the bridge at 1.025 s). The effect of the rougher profiles on the IMFs has been to increase the amplitude of the spikes and their number (in agreement with an increase in number of stiffness changes).

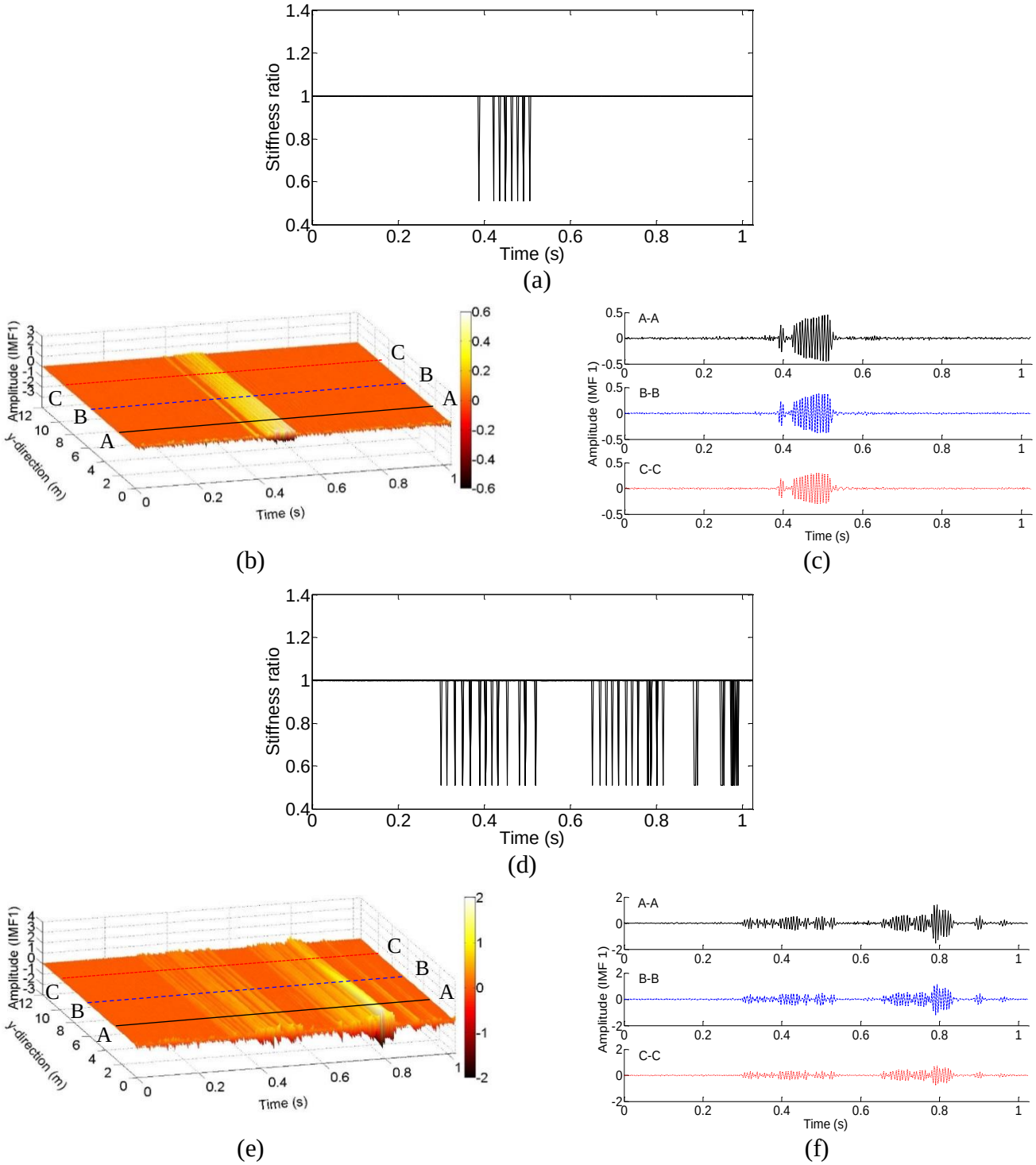

Fig. 23. IMF1s using EEMD of accelerations at mid-span for a plate model with a localised elasto-plastic response at 9 m and different road profiles: (a) True variation of longitudinal stiffness ratio at elements along the width of the bridge at 9 m from left support with time using road class 'C', (b) IMF1 amplitude versus time across the bridge width using road class 'C', (c) Three sections across (b), (d) True variation of longitudinal stiffness ratio at 9 m from left support with time using road class 'E', (e) IMF1 amplitude versus time across the bridge width using road class 'E', (f) Three sections across (e).

3.5 Impact of Vehicle Speed

The speed of the vehicle travelling over the bridge is a key parameter that influences both the bridge vibrations and duration of the signal. Fig. 24(a) shows the true variation of stiffness ratio at all the elements along the width of the bridge at 9 m from left support with time for the same bridge scenario of Figs. 22(a) to (c), except this time the vehicle is driven at a slower speed of 10 m/s. The time instances where stiffness changes take place from 0.87 to 1 s and from 1.2 to 1.55 s (Fig. 24(a)). Figs. 24(b) and (c) show IMF1 is able to recognise the same time instances of Fig. 24(a) for any transverse location of an accelerometer across mid-span, although higher amplitudes of the spikes can be observed for measurement locations closer to the vehicle path. For a speed of 30 m/s (Figs. 24(d), (e) and (f)), the signal is shortened with respect to 10 m/s, but unlike processing by wavelet analysis, the performance of EEMD is not affected by the signal length. It is still possible to find a good agreement between the targeted changes in Fig. 24(d) (approximately between 0.31 and 0.51 s) and the spikes of the IMFs in Figs. 24(e) and (f).

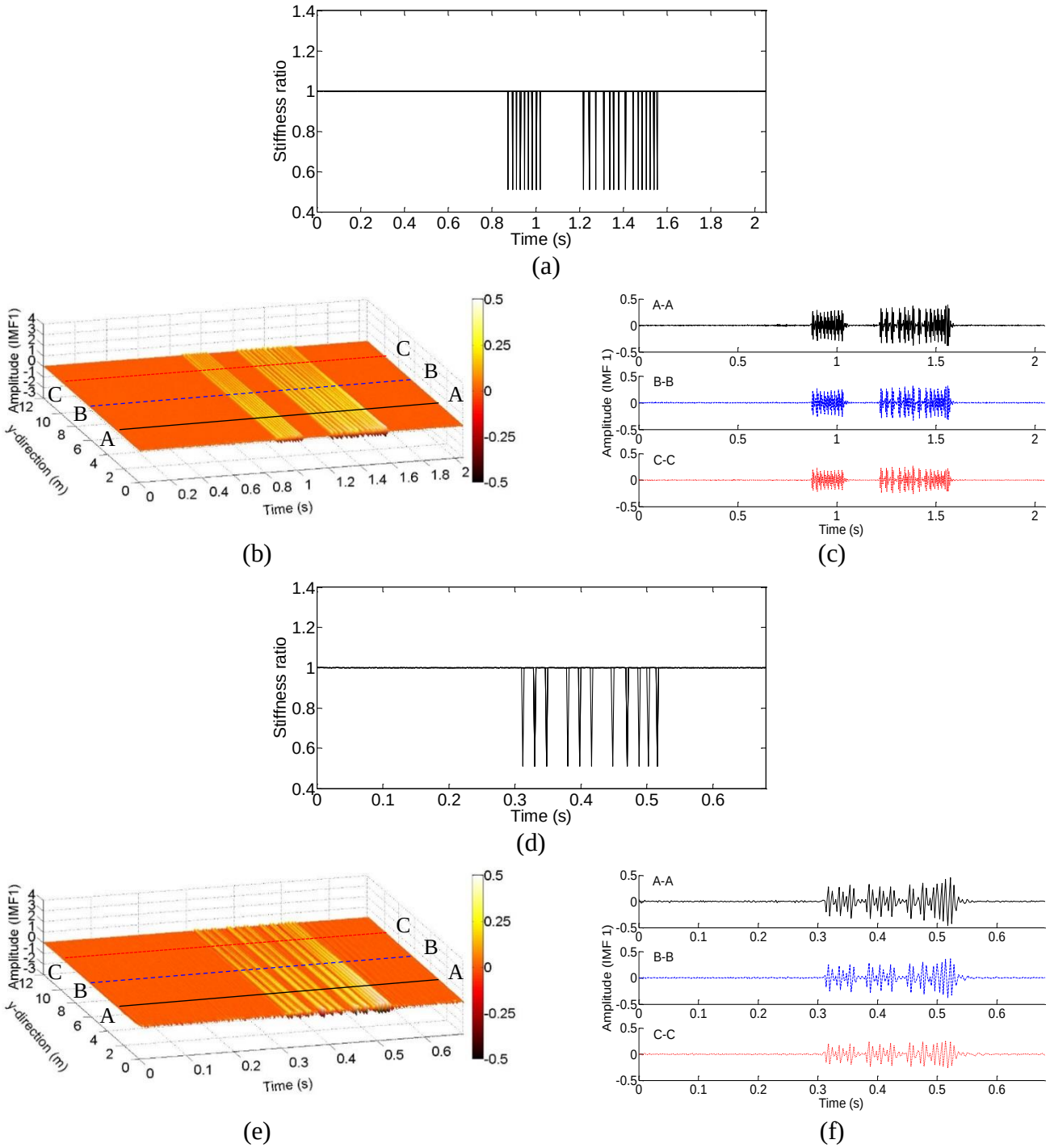

Fig. 24. IMF1 using EEMD of accelerations at mid-span for a plate model with a localised elasto-plastic response at 9 m traversed by a vehicle at different speeds: (a) True variation of longitudinal stiffness ratio at all elements along the width of the bridge at 9 m from left support with time at 10 m/s, (b) IMF1 amplitude versus time across the bridge width at 10 m/s, (c) Three sections across (b), (d) True variation of

longitudinal stiffness ratio at 9 m from left support with time at 30 m/s, (e) IMF1 amplitude versus time across the bridge width at 30 m/s, (f) Three sections across (e).

3.6 Impact of noise

Up to this point, all VBI simulations have ignored the presence of noise in the theoretical acceleration response. In practise, true measurements from field tests will contain noise. For that reason, the theoretical noise-free signal is corrupted here using the additive noise model [34]:

$$\{\ddot{u}_{bn}(t)\} = \{\ddot{u}_b(t)\} + n_l\{N\}\sigma \tag{14}$$

where $\{\ddot{u}_{bn}(t)\}$ is the acceleration corrupted by noise, $\{\ddot{u}_b(t)\}$ is the acceleration of the bridge at time t, n_l is the noise level, $\{N\}$ is the standard normal distribution vector with zero mean and unit standard deviation and σ is the standard deviation of the noise-free signal.

This additive noise model is the same employed by the EEMD method to calculate the noise amplitude that maximises the relative *RMSE* (Equation (9)). The difference between the noise added to corrupt the acceleration signal and the noise added in step 1 of EEMD illustrated in Fig. 8, lies on that the level of noise is random and have no specific value in the first case while the noise level used in the EEMD method is chosen based on maximising the *RMSE*. The acceleration corrupted with 5% noise level (i.e., n_l = 0.05 in Equation (14)) is shown in time and frequency domains in Figs. 25(a) and (b) respectively. This noisy response is clearly less smooth than the one shown in Fig. 15 for a noise-free response. The PSD still clearly gives first and second natural frequencies of 8.03 Hz and 17.3 Hz respectively.

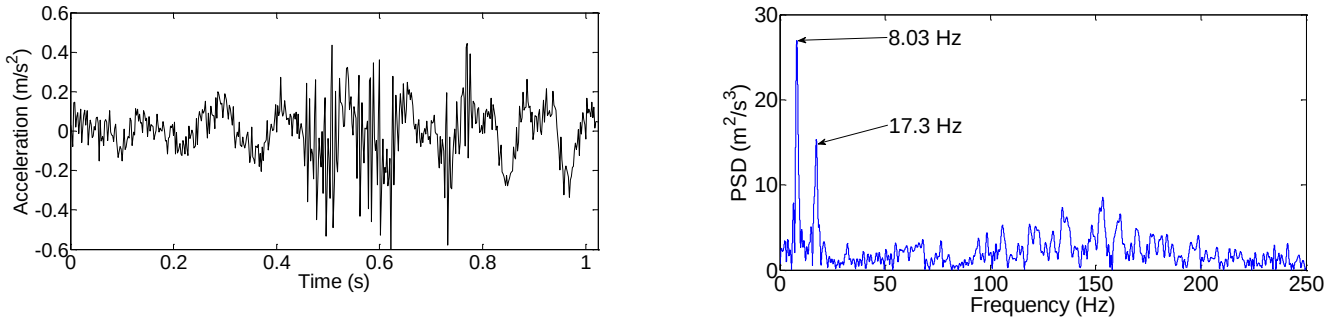

(a) (b)

Fig. 25. Mid-span acceleration response (at 3 m from bridge centreline in lane 1) corrupted with 5% noise versus time of a bridge with an elasto-plastic region at 9 m: (a) time domain; (b) frequency domain

By applying the EEMD method with optimal noise amplitude (i.e., maximizing Equation (9)), and an ensemble number equal to 100 trials, the IMFs are calculated and plotted in Fig. 26. IMF1 ($c_1(t)$) captures peaks related to stiffness changes in the intervals 0.45-0.5 s, 0.55-0.62 s, and 0.72-0.76 s (in agreement with true stiffness changes shown in Fig. 16) and other peaks of smaller magnitude related to noise that was not present in previous sections. IMF2 ($c_2(t)$) and IMF3 ($c_3(t)$) contain frequency content of the VBI system and noise mixed with some elasto-plastic related frequency content. The first mode of vibration of the bridge in the 'healthy' state is captured by $c_5(t)$ and $c_6(t)$ which is similar to what has been seen in Fig. 17 for acceleration without noise.

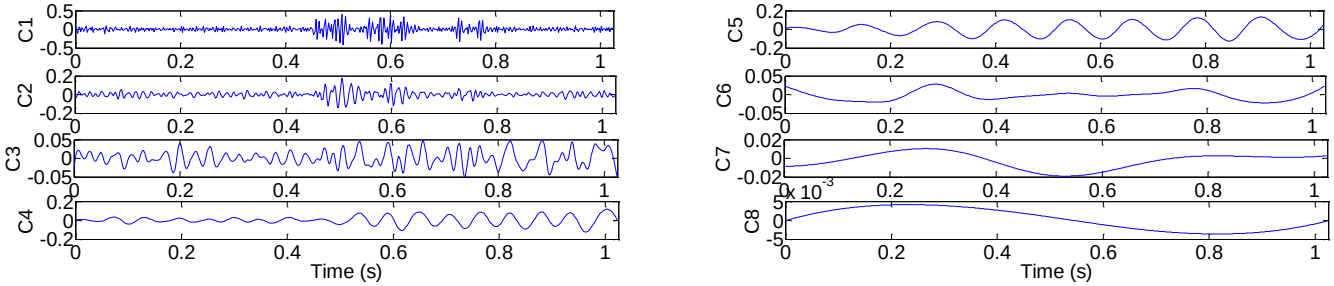

Fig. 26. IMFs of mid-span acceleration response (3 m from bridge centreline in lane 1) corrupted with 5% noise in the case of a structure with a localised elasto-plastic response at 9 m

The same theoretical acceleration response is further corrupted with a 10% noise level (n_l = 0.10 in Equation (12)) and the resulting IMFs are shown in Fig. 27. In spite of the significant noise, the relevant peaks in IMF1 denoting stiffness changes have the largest amplitude and are distinguishable, although they do not stand above the others as clearly as before. As in Fig. 26, $c_2(t)$ and $c_3(t)$ contain elasto-plastic related frequency content mixed at similar amplitudes with noise and high frequency content of the VBI system which does not make them suitable for identifying sudden stiffness changes. $c_5(t)$ and $c_6(t)$ contain the main modes of vibration of the bridge and the rest of the IMFs ($c_7(t)$ and $c_8(t)$) are residues of lower frequencies, i.e., related to the static component of the response.

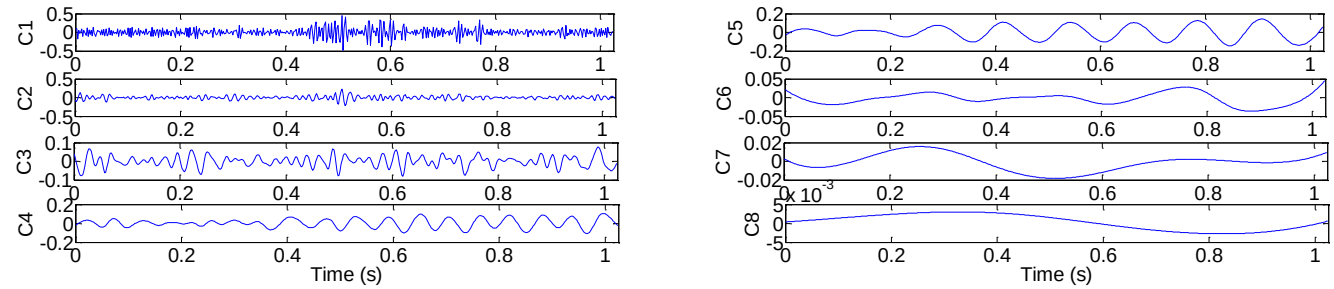

Fig. 27. IMFs of mid-span acceleration response (3 m from bridge centreline in lane 1) corrupted with 10% noise in the case of a structure with a localised elasto-plastic response at 9 m

From the figures above, it is evident that noise has some impact on the performance of EEMD, but the frequency content related to the elasto-plastic region appears to be successfully separated from other undesired high frequency components even for a 10% noise.

4. Conclusions

Past research has employed wavelet analysis and EMD to identify a stiffness change from the response of a structure to a moving load, however, these methods have been applied to perfectly linear elastic systems and they have shown to be severely limited by the roughness of the road profile, the vehicle speed and the level of noise. In this paper, the EEMD method has been applied to the mid-span acceleration response of a bridge model to demonstrate its capability in identifying brief stiffness changes even with rough profiles, high vehicle speeds and noisy signals. The change in stiffness has been modelled using a bi-linear hysteretic moment-curvature relationship at selected finite elements. In this model, the stiffness returns to its original value at unloading, i.e., stiffness changes happen in short time windows that make difficult its identification using only a frequency analysis. The IMF1 obtained using EEMD has been shown to successfully separate the elasto-plastic response component in these short windows from other frequency components of the VBI system. Spikes have been clearly distinguished in the IMF1 at instants of stiffness changes for different extents of the elasto-plastic region (full-width, half-width and localised at one single element) and transverse locations of the simulated accelerations. Exceptions are made for the case of using acceleration responses far from small localised regions. The closer the accelerometer is to the elasto-plastic region and the higher is the

stiffness loss, the higher the amplitudes of the spikes identified in IMF1 have become. As expected, higher spike amplitudes have been observed in mid-span measurement locations in lane 1, where the vehicle is travelling and where the elasto-plastic region is located. The influence of the road profile, speed of the moving vehicle and noise on the identification of stiffness changes by EEMD have also been tested, and in all cases, the IMF1 has been able to identify the instants at which changes take place and their approximated duration. From this investigation, the authors conclude that the EEMD method has shown considerable potential as a future tool for damage detection applications.

Acknowledgements

The authors would like to thank the funding received from the GREP Scholarship for 'PhD in Sustainable Development Programme' at University College Dublin.

References

[1] A. González and D. Hester, "An investigation into the acceleration response of a damaged beam-type structure to a moving force," *Journal of Sound and Vibration,* vol. 332, pp. 3201-3217, 2013.

[2] A. Kunwar, R. Jha, M. Whelan, and K. Janoyan, "Damage detection in an experimental bridge model using Hilbert–Huang transform of transient vibrations," *Structural Control and Health Monitoring,* vol. 20, pp. 1-15, 2013.

[3] P. Cornwell, C. R. Farrar, S. W. Doebling, and H. Sohn, "Environmental variability of modal properties," *Experimental Techniques,* vol. 23, pp. 45-48, 2008.

[4] D. Hester and A. Gonzalez, "A wavelet-based damage detection algorithm based on bridge acceleration response to a vehicle," *Mechanical Systems and Signal Processing,* vol. 28, pp. 145-166, 2012.

[5] C. Wang, W.-X. Ren, Z.-C. Wang, and H.-P. Zhu, "Instantaneous frequency identification of time-varying structures by continuous wavelet transform," *Engineering Structures,* vol. 52, pp. 17-25, 2013.

[6] E. N. Chatzi and A. W. Smyth, "The unscented Kalman filter and particle filter methods for nonlinear structural system identification with non-collocated heterogeneous sensing," *Structural Control and Health Monitoring,* vol. 16, pp. 99-123, 2009.

[7] M. Wu and A. W. Smyth, "Application of the unscented Kalman filter for real-time nonlinear structural system identification," *Structural Control and Health Monitoring,* vol. 14, pp. 971-990, 2007.

[8] N. E. Huang, Z. Shen, S. R. Long, M. C. Wu, H. H. Shih, Q. Zheng, N. C. Yen, C. C. Tung, and H. H. Liu, "The empirical mode decomposition and the Hilbert spectrum for nonlinear and non-stationary time series analysis," *Proceedings of the Royal Society of London. Series A: Mathematical, Physical and Engineering Sciences,* vol. 454, pp. 903-995, 1998.

[9] P. Frank Pai, "Instantaneous frequency of an arbitrary signal," *International Journal of Mechanical Sciences,* vol. 52, pp. 1682-1693, 2010.

[10] N. E. Huang and S. S. Shen, *Hilbert-Huang transform and its applications*. Singapore; Hackensack, NJ; London: World Scientific, 2005.

[11] G. Kerschen, A. F. Vakakis, Y. Lee, D. McFarland, and L. Bergman, "Toward a fundamental understanding of the Hilbert-Huang transform in nonlinear structural dynamics," *Journal of Vibration and Control,* vol. 14, pp. 77-105, 2008.

[12] Z. K. Peng, P. W. Tse, and F. L. Chu, "An improved Hilbert–Huang transform and its application in vibration signal analysis," *Journal of Sound and Vibration,* vol. 286, pp. 187-205, 2005.

[13] N. Roveri and A. Carcaterra, "Damage detection in structures under traveling loads by Hilbert–Huang transform," *Mechanical Systems and Signal Processing,* vol. 28, pp. 128-144, 2012.

[14] Z. Wu and N. E. Huang, "Ensemble empirical mode decomposition: a noise-assisted data analysis method," *Advances in adaptive data analysis,* vol. 1, pp. 1-41, 2009.

[15] J. Zheng, J. Cheng, and Y. Yang, "Partly ensemble empirical mode decomposition: An improved noise-assisted method for eliminating mode mixing," *Signal Processing*, vol. 96, Part B, pp. 362-374, 2014.
[16] X. An, D. Jiang, S. Li, and M. Zhao, "Application of the ensemble empirical mode decomposition and Hilbert transform to pedestal looseness study of direct-drive wind turbine," *Energy*, vol. 36, pp. 5508-5520, 2011.
[17] Y. Zhang and Z. Xie, "Ensemble empirical mode decomposition of impact-echo data for testing concrete structures," *NDT & E International*, vol. 51, pp. 74-84, 2012.
[18] J. Meredith, A. González, and D. Hester, "Empirical Mode Decomposition of the acceleration response of a prismatic beam subject to a moving load to identify multiple damage locations," *Shock and Vibration*, vol. 19, pp. 845-856, 2012.
[19] A. V. Lopes, S. M. R. Lopes, and R. N. F. do Carmo, "Effects of the compressive reinforcement buckling on the ductility of RC beams in bending," *Engineering Structures*, vol. 37, pp. 14-23, 2012.
[20] T. Lou, S. M. R. Lopes, and A. V. Lopes, "Nonlinear and time-dependent analysis of continuous unbonded prestressed concrete beams," *Computers & Structures*, vol. 119, pp. 166-176, 2013.
[21] M. G. Santoro and S. K. Kunnath, "Damage-based RC beam element for nonlinear structural analysis," *Engineering Structures*, vol. 49, pp. 733-742, 2013.
[22] W.-F. Chen and L. Duan, *Bridge engineering: seismic design*: CRC Press, 2003.
[23] A. González, E. J. OBrien, and P. J. McGetrick, "Identification of damping in a bridge using a moving instrumented vehicle," *Journal of Sound and Vibration*, vol. 331, pp. 4115-4131, 2012.
[24] L. Frýba, *Vibration of solids and structures under moving loads*: Thomas Telford, 1999.
[25] C. W. Rowley, L. "Moving force identification of axle forces on bridges," PhD thesis, School of Architecture, Landscape and Civil Engineering, University College Dublin, Dublin, 2007.[26] K. Pugasap, "Hysteresis Based Model Prediction of Integral Abutment Bridge Behaviour," PhD thesis, College of Engineering, Pennsylvania State University, Pennsylvania, 2006.
[27] M. Zeynalian, H. R. Ronagh, and P. Dux, "Analytical Description of Pinching, Degrading, and Sliding in a Bilinear Hysteretic System," *Journal of engineering mechanics*, vol. 138, pp. 1381-1387, 2012.
[28] N. Mostaghel and R. A. Byrd, "Analytical description of multidegree bilinear hysteretic system " *Journal of engineering mechanics*, vol. 126, p. 588, 2000.
[29] H.-G. Kwak and S.-P. Kim, "Nonlinear analysis of RC beams based on moment–curvature relation," *Computers & Structures*, vol. 80, pp. 615-628, 2002.
[30] S. Dobson, M. Noori, Z. Hou, M. Dimentberg, and T. Baber, "Modeling and random vibration analysis of SDOF systems with asymmetric hysteresis," *International Journal of Non-Linear Mechanics*, vol. 32, pp. 669-680, 1997.
[31] M. Kikuchi and I. D. Aiken, "An Analytical Hysteresis Model for Elastomeric Seismic Isolation Bearings," *Earthquake engineering & structural dynamics*, vol. 26, pp. 215-231, 1997.
[32] J. Song and A. Der Kiureghian, "Generalized Bouc–Wen model for highly asymmetric hysteresis," *Journal of engineering mechanics*, vol. 132, pp. 610-618, 2006.
[33] Y.-K. Wen, "Method for random vibration of hysteretic systems," *Journal of the Engineering Mechanics Division*, vol. 102, pp. 249-263, 1976.
[34] F. Y. Cheng, *Matrix analysis of structural dynamics: applications and earthquake engineering*: CRC Press, 2000.
[35] X. Zhu and S. Law, "Wavelet-based crack identification of bridge beam from operational deflection time history," *International Journal of Solids and Structures*, vol. 43, pp. 2299-2317, 2006.
[36] J. N. Yang, Y. Lei, S. Lin, and N. Huang, "Hilbert-Huang based approach for structural damage detection," *Journal of engineering mechanics*, vol. 130, pp. 85-95, 2003.
[37] Y. L. Xu and J. Chen, "Structural Damage Detection Using Empirical Mode Decomposition: Experimental Investigation," *Journal of engineering mechanics*, vol. 130, pp. 1279-1288, 2004.
[38] W. Guo and P. W. Tse, "A novel signal compression method based on optimal ensemble empirical mode decomposition for bearing vibration signals," *Journal of Sound and Vibration*, vol. 332, pp. 423-441, 2013.
[39] D. Cantero, E. J. OBrien, and A. González, "Modelling the vehicle in vehicle–infrastructure dynamic interaction studies," *Proceedings of the Institution of Mechanical Engineers, Part K: Journal of Multi-body Dynamics*, vol. 224, pp. 243-248, 2010.

[40] E. J. OBrien, D. Cantero, B. Enright, and A. González, "Characteristic Dynamic Increment for extreme traffic loading events on short and medium span highway bridges," *Engineering Structures*, vol. 32, pp. 3827-3835, 2010.
[41] A. González, "Vehicle-bridge dynamic interaction using finite element modelling", *Finite Element Analysis*, David Moratal (Ed.), InTech, available from http://www.intechopen.com/books/finite-element-analysis/vehicle-bridge-dynamic-interaction-using-finite-element-modelling, pp. 637-662, 2010.
[42] D. Cantero, A. González, and E. J. OBrien, "Comparison of bridge dynamics due to articulated 5-axle trucks and large cranes," *The Baltic Journal of Road and Bridge Engineering*, vol. Vol. 6, pp. 39-47, 2011.
[43] M. F. Green, D. Cebon, and D. J. Cole, "Effects of vehicle suspension design on dynamics of highway bridges," *Journal of Structural Engineering*, vol. 121, p. 272, 1995.
[44] J. N. Reddy, *Energy and Variational Methods in Applied Mechanics*: Wiley, 1984.
[45] A. Gonzalez, *Development of accurate methods of weighing trucks in motion*: LAP Lambert Academic Publishing AG & Co. KG, 2010.
[46] P. H. Kirkegaard, S. R. K. Nielsen, and I. Enevoldsen, *Heavy Vehicles on Minor Highway Bridges: Calculation of Dynamic Impact Factors from Selected Crossing Scenarios*: Instituttet for Bygningsteknik, Aalborg Universitet, 1997.
[47] A. González, E. J. OBrien, D. Cantero, Y. Li, J. Dowling, and A. Žnidarič, "Critical speed for the dynamics of truck events on bridges with a smooth road surface," *Journal of Sound and Vibration*, vol. 329, pp. 2127-2146, 2010.
[48] ISO, "ISO 8608 Mechanical vibration-Road surface profiles-Reporting of measured data," ed. Switzerland: International Organization for Standardization, 1995.
[49] D. Cebon, and D.E. Newland, "Artificial generation of road surface topography by the inverse F.F.T. method," *Vehicle System Dynamics*, Vol. 12, pp. 160-165, 1983.
[50] N. K. Harris, E. J. OBrien, and A. González, "Reduction of bridge dynamic amplification through adjustment of vehicle suspension damping," *Journal of Sound and Vibration*, vol. 302, pp. 471-485, 2007.
[51] P. K. McGetrick, C.-W.; González, A.; , "Dynamic axle force and road profile identification using a moving vehicle," *International Journal of Architecture, Engineering and Construction*, vol. 2, pp. 1-16, 2013.
[52] J. Dowling, A. González, E. J. OBrien, and B. Jacob, "Experimental Testing of a Multiple Sensor Bridge Weigh-in Motion Algorithm in an Integral Bridge," in *6th International Conference on Weigh-In-Motion (ICWIM 6)*, 2012.
[53] P. H. Rattigan, "The Assessment of Bridge Traffic Loading Allowing for Vehicle-Bridge Dynamic Interaction," PhD thesis, School of Architecture, Landscape and Civil Engineering, University College Dublin, Dublin, Ireland, 2007.

Appendix A

This Appendix describes the non-linear plate element used in simulations at selected locations. Fig. A.1(a) shows the moments (M_x, M_y and M_{xy}) and vertical forces (V) acting at the four nodes, labelled i, j, k and l of a plate element. Each node has four DOFs defining rotations (θ_{xi}, θ_{yi} and θ_{xyi}) and displacements (u_i is the vertical displacement at node i) as shown in Fig. A.1(b) for the linear component and in Fig. A.1(c) for the elasto-plastic component (only node k is shown for illustration purposes).

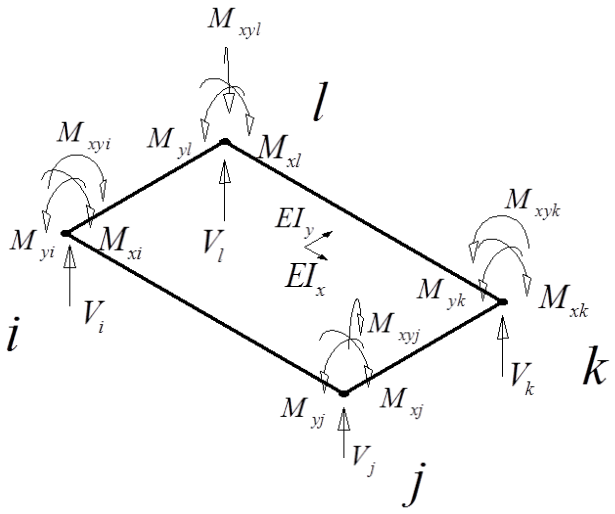

(a)

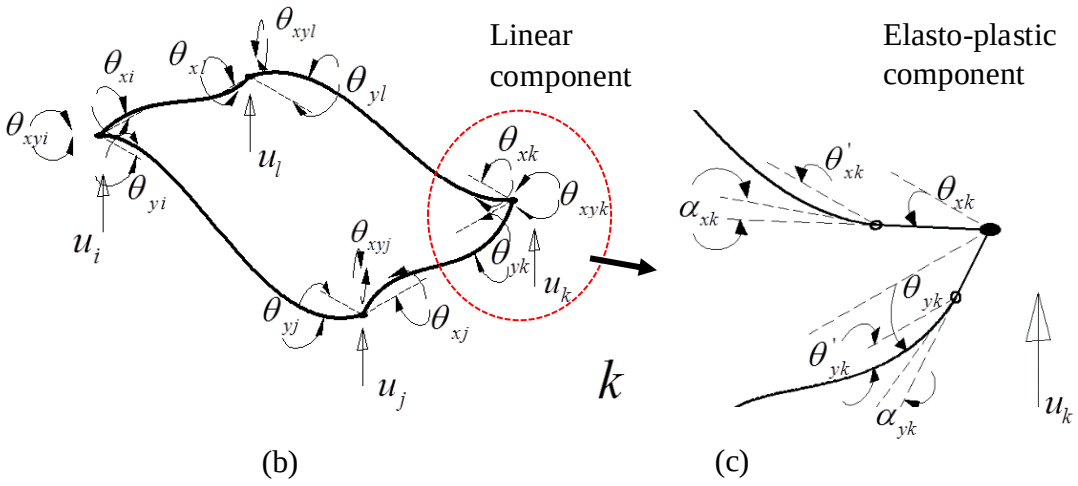

(b) (c)

Fig. A.1. (a) Moments and shear forces acting on the plate element; (b) linear component of DOFs and (c) elasto-plastic component of DOFs

The elasto-plastic component in Fig. A.1(c) shows the rotations ($\theta'_{xk}, \theta'_{yk}$ and θ'_{xyk}) and plastic angles (α_{xk}, α_{yk} and α_{xyk}) associated to node *k* (α_{xyk}, θ_{xyk} and θ'_{xyk} are not shown in the figure for clarity) given by:

$$\alpha_{xk} \neq 0; \quad \alpha_{yk} \neq 0; \quad \alpha_{xyk} \neq 0 \tag{A.1}$$

$$\theta'_{xk} = \theta_{xk} - \alpha_{xk}; \quad \theta'_{yk} = \theta_{yk} - \alpha_{yk}; \quad \theta'_{xyk} = \theta_{xyk} - \alpha_{xyk} \tag{A.2}$$

In Equation A.1, α_{xk}, α_{yk} and α_{xyk} are the plastic angles which are the difference between the elasto-plastic component and the linear component. For α_{xyk}, subscripts *x*, *y* and *k* indicate the x-direction, y-direction, and node *k* respectively. In Equation A.2, $\theta'_{xk}, \theta'_{yk}$ and θ'_{xyk} are the end rotations of the elasto-plastic component and θ_{xk}, θ_{yk} and θ_{xyk} are the end rotations of the linear component.

Moments and forces acting on the non-linear plate element are assumed to be subjected to three possible states:

1. All nodes are linear

2. Nodes *i* and *l* are nonlinear
3. Nodes *j* and *k* are nonlinear

In states 2 and 3, a state of yield has been reached (i.e., where the bending moment in the element exceeds the yield bending moment). For state 1, the stiffness matrix is linear and it is simply the elementary 16x16 stiffness matrix $[K_e]$ given by Equation (A.3).

$$[K_e] = \int_0^b \int_0^a [[C][H]^{-1}]^T [D][[C][H]^{-1}] dxdy \tag{A.3}$$

In Equation A.3, the matrix $[C]$ is given by:

$$[C] = [B][H]$$

where $[B]$ is the strain displacement matrix, $[H]$ is a 16×16 matrix that contains the lengths of the plate in the x- and y- directions (a is the length of the plate in x-direction and b is the length of the plate in y-direction respectively) which is commonly found in orthotropic plate elements, and $[D]$ is the constitutive matrix for an orthotropic plate given by:

$$[D] = \begin{bmatrix} D11 & D12 & 0 \\ D12 & D22 & 0 \\ 0 & 0 & D66 \end{bmatrix}$$

where $D11$, $D12$ and $D22$ contain the Young's modulus and Poisson's ratio in the x- and -y directions, and $D66$ contains the Young's modulus in the x-y direction. Further details on the derivation of the coefficients of the matrix $[K_e]$ can be found in [53].

For the condition where all nodes are linear, the rotations and plastic angles in Equations (A.1) and (A.2) become:

$$\alpha_{xk} = 0; \quad \alpha_{yk} = 0; \quad \alpha_{xyk} = 0 \tag{A.4}$$

$$\theta'_{xk} = \theta_{xk}; \quad \theta'_{yk} = \theta_{yk}; \quad \theta'_{xyk} = \theta_{xyk} \tag{A.5}$$

For the nonlinear states 2 and 3, the elemental stiffness matrix can be derived by expressing plastic angles (α_x, α_y and α_{xy}) in terms of the rotations and displacements. Since the moments applied to the elasto-plastic components of the DOFs of a nonlinear node are constant, an increase in moments M_x, M_y and M_{xy} at any node are due to M_{px}, M_{py} and M_{pxy}, which are the moments applied to the linear component of the DOFs. This can be written in incremental form as:

$$\Delta M_x = \Delta M_{px}; \quad \Delta M_y = \Delta M_{py}; \quad \Delta M_{xy} = \Delta M_{pxy} \tag{A.6}$$

From Equation (A.6), the α's can be determined in terms of rotations and displacements (shown in Equation (A.7) for nodes *i* and *l*).

$$\begin{Bmatrix} \alpha_{xi} \\ \alpha_{yi} \\ \alpha_{xyi} \\ \alpha_{xl} \\ \alpha_{yl} \\ \alpha_{xyl} \end{Bmatrix} = \underbrace{\begin{bmatrix} b_2 & c_2 & d_2 & n_2 & o_2 & r_2 \\ b_3 & c_3 & d_3 & n_3 & o_3 & r_3 \\ b_4 & c_4 & d_4 & n_4 & o_4 & r_4 \\ b_{14} & c_{14} & d_{14} & n_{14} & o_{14} & r_{14} \\ b_{15} & c_{15} & d_{15} & n_{15} & o_{15} & r_{15} \\ b_{16} & c_{16} & d_{16} & n_{16} & o_{16} & r_{16} \end{bmatrix}}_{[R]} \underbrace{\begin{Bmatrix} A_2 \\ A_3 \\ A_4 \\ A_{14} \\ A_{15} \\ A_{16} \end{Bmatrix}}_{\{A\}} \tag{A.7}$$

In Equation (A.7), the values of matrix [R] correspond to stiffness values of the nonlinear nodes i and l. They are extracted from the elemental stiffness matrix ([K_e]) of a plate defined in Equation (A.3) and are given by:

$$b_2 = 52/35*a/b*D22+8/25/a*b*D12+16/25/a*b*D66+4/35/a^3*D11*b^3$$
$$b_3 = -61/50*D12-11/35/a^2*b^2*D11-1/25*D66-11/35/b^2*D22*a^2$$
$$b_4 = -22/105*a^2/b*D22-4/25*D12*b-4/75*b*D66-2/35/a^2*b^3*D11$$
$$b_{14} = -4/25/a*b*D66+26/35*a/b*D22-3/35/a^3*D11*b^3-2/25/a*b*D12$$
$$b_{15} = 3/25*D12+1/25*D66+11/35/b^2*D22*a^2-13/70/a^2*b^2*D11$$
$$b_{16} = -11/105*a^2/b*D22+1/25*D12*b+1/75*b*D66+3/70/a^2*b^3*D11$$
$$c_2 = -11/105*a^2/b*D22+1/25*D12*b+1/75*b*D66+3/70/a^2*b^3*D11$$
$$c_3 = 52/35/a*b*D11+8/25*a/b*D12+16/25*a/b*D66+4/35/b^3*D22*a^3$$
$$c_4 = 22/105/a*b^2*D11+4/25*D12*a+2/35/b^2*D22*a^3+4/75*a*D66$$
$$c_{14} = -1/25*D66-11/35/b^2*D22*a^2+13/70/a^2*b^2*D11-3/25*D12$$
$$c_{15} = 18/35/a*b*D11-8/25*a/b*D12-16/25*a/b*D66-4/35/b^3*D22*a^3$$
$$c_{16} = -13/105/a*b^2*D11+2/75*D12*a+4/75*a*D66+2/35/b^2*D22*a^3$$
$$d_2 = -22/105*a^2/b*D22-4/25*D12*b-4/75*b*D66-2/35/a^2*b^3*D11$$
$$d_3 = 22/105/a*b^2*D11+4/25*D12*a+2/35/b^2*D22*a^3+4/75*a*D66$$
$$d_4 = 4/105/a*D11*b^3+8/225*D12*a*b+16/225*a*b*D66+4/105*a^3/b*D22$$
$$d_{14} = -11/105*a^2/b*D22+1/25*D12*b+1/75*b*D66+3/70/a^2*b^3*D11$$
$$d_{15} = 13/105/a*b^2*D11-2/75*D12*a-4/75*a*D66-2/35/b^2*D22*a^3$$
$$d_{16} = 2/105*a^3/b*D22-4/225*a*b*D66-1/35/a*D11*b^3-2/225*D12*a*b$$
$$n_2 = -4/25/a*b*D66+26/35*a/b*D22-3/35/a^3*D11*b^3-2/25/a*b*D12$$
$$n_3 = -1/25*D66-11/35/b^2*D22*a^2+13/70/a^2*b^2*D11-3/25*D12$$
$$n_4 = -11/105*a^2/b*D22+1/25*D12*b+1/75*b*D66+3/70/a^2*b^3*D11$$

$$n_{14} = 52/35*a/b*D22 + 8/25/a*b*D12 + 16/25/a*b*D66 + 4/35/a^3*D11*b^3$$
$$n_{15} = 11/35/a^2*b^2*D11 + 61/50*D12 + 1/25*D66 + 11/35/b^2*D22*a^2$$
$$n_{16} = -22/105*a^2/b*D22 - 4/25*D12*b - 4/75*b*D66 - 2/35/a^2*b^3*D11$$
$$o_2 = 3/25*D12 + 1/25*D66 + 11/35/b^2*D22*a^2 - 13/70/a^2*b^2*D11$$
$$o_3 = 18/35/a*b*D11 - 8/25*a/b*D12 - 16/25*a/b*D66 - 4/35/b^3*D22*a^3$$
$$o_4 = 13/105/a*b^2*D11 - 2/75*D12*a - 4/75*a*D66 - 2/35/b^2*D22*a^3$$
$$o_{14} = 11/35/a^2*b^2*D11 + 61/50*D12 + 1/25*D66 + 11/35/b^2*D22*a^2$$
$$o_{15} = 52/35/a*b*D11 + 8/25*a/b*D12 + 16/25*a/b*D66 + 4/35/b^3*D22*a^3$$
$$o_{16} = -4/75*a*D66 - 22/105/a*b^2*D11 - 2/35/b^2*D22*a^3 - 4/25*D12*a$$
$$r_2 = -11/105*a^2/b*D22 + 1/25*D12*b + 1/75*b*D66 + 3/70/a^2*b^3*D11$$
$$r_3 = -13/105/a*b^2*D11 + 2/75*D12*a + 4/75*a*D66 + 2/35/b^2*D22*a^3$$
$$r_4 = 2/105*a^3/b*D22 - 4/225*a*b*D66 - 1/35/a*D11*b^3 - 2/225*D12*a*b$$
$$r_{14} = -22/105*a^2/b*D22 - 4/25*D12*b - 4/75*b*D66 - 2/35/a^2*b^3*D11$$
$$r_{15} = -4/75*a*D66 - 22/105/a*b^2*D11 - 2/35/b^2*D22*a^3 - 4/25*D12*a$$
$$r_{16} = 4/105/a*D11*b^3 + 8/225*D12*a*b + 16/225*a*b*D66 + 4/105*a^3/b*D22$$

Matrix [*A*] can be written in the form:

$$[A] = \{A_n\} \tag{A.8}$$

where n = [2,3,4,14,15,16], corresponding to nodes *i* and *l* and:

$$A_n = \{a_n\ b_n\ c_n\ d_n\ e_n\ f_n\ g_n\ h_n\ i_n\ j_n\ k_n\ l_n\ m_n\ n_n\ o_n\ r_n\} \tag{A.9}$$

The α's in Equation (A.7) are shown for node *i* and *l*(i.e., an element where the left nodes are nonlinear). From Equation (A.8), the nonlinear elemental stiffness matrix for an element can be written as:

$$[K_{enl}] = \left[[K_e] - q[S][R]^{-1}[A]\right] \tag{A.10}$$

where $[K_{enl}]$ is the nonlinear stiffness matrix of an element where left nodes are nonlinear, q is the post-yield stiffness value (Section 2.1) and [*S*] is given by:

$$[S] = [A]^t \tag{A.11}$$

where $[A]^t$ is the transpose of matrix [*A*]. Equation (A.11) can be modified to include any node that has a nonlinear stiffness by simply varying the corresponding nodal values in matrix [*S*], [*A*] and [*R*].

In modelling the elasto-plastic response of selected elements, Equation (A.10) is used to obtain their elemental stiffness matrix where left nodes are nonlinear (n = [2,3,4,14,15,16]). For elements where right nodes are nonlinear, n becomes n = [6,7,8,10,11,12] which correspond to nodes *j* and *k* in Fig. A.1. The approach can be modified to include a smooth transition and more complicated hysteresis behaviour such as

the Bouc-Wen model. The elemental stiffness matrix remains the same and only post-yield stiffness value (q) needs to be varied depending on the moment-curvature relationship.